



Characterization of pore space in Permo-Triassic sandstone from SW-Germany using the anisotropy of magnetic susceptibility

Agnes Kontny¹ · Benjamin Busch¹ · Julius Schenk¹ · Ilnar Khasanov^{1,2}

Received: 10 January 2023 / Accepted: 19 September 2023 / Published online: 19 October 2023
© The Author(s) 2023

Abstract

Pore space in siliciclastic rocks is one of the most important petrophysical properties in geothermal and hydrocarbon reservoir rock characterization. We used the anisotropy of magnetic susceptibility (AMS) of ferrofluid-impregnated Permo-Triassic sandstones of different Buntsandstein and Rotliegend facies as a proxy for pore space anisotropy and preferred flow direction as a case study for reservoir characterization. We compared the calculated ferrofluid porosity (2–21%) with He porosity (2–26%) and permeability (0.002–214 mD) and described the sediment microstructure using petrographic point-counting analysis. For water- and oil-based ferrofluid impregnation, we observed a positive correlation with He porosity and mass and susceptibility impregnation efficiency were used to control the quality of the impregnation process. Triaxial to oblate magnetic rock fabrics were mostly mimicked by the magnetic pore fabrics, except for some of the water-based ferrofluid impregnated samples, where magnetic ellipsoid shapes changed from oblate to prolate. AMS of the unimpregnated sandstones reflects well defined primary sedimentary to diagenetic fabrics with grain imbrication and cross bedding along with more laminated sedimentary structures. Deviation in ferrofluid-impregnated AMS axes orientation can be related either to the low anisotropy < 1.07 in sandstones from the Lower and Upper Buntsandstein, or the low impregnation efficiency. The mimicry is mostly better when the magnetic susceptibility of the sandstone is higher due to a higher concentration of phyllosilicates while micro-porosity is controlled by the clay fabric. A comparison of sediment petrography with magnetic pore fabrics suggests that the pore space is controlled by the bedding of the sandstones with mostly no preferred flow direction within the bedding plane.

Keywords Magnetic pore fabric · Permo-Triassic sandstone · SW-Germany · Ferrofluid porosity · He porosity · Permeability

Introduction

Besides permeability, the pore space in siliciclastic rocks is one of the most important petrophysical properties in reservoir rock characterization (Blackbourn 2012; Parés et al. 2016). Standard porosity measurements give the volumetric fraction of voids in a rock but cannot give any information on the 3D pore space geometry or orientation. As pore space orientation is of particular interest for fluid

flow, e.g., in geothermal, hydrocarbon or gas storage reservoirs, the assessment of permeability for the purpose of reservoir model development requires microstructural rock descriptions and petrophysical measurements. Especially, the preferred orientation of the long pores axes is a crucial controlling parameter for the direction of maximum permeability in intact unfractured sandstones. The anisotropy of the pore space is therefore critical for the description of fluid pathways.

Bedding as a primary sedimentary structure in a sandstone will likely represent the preferred plane for fluid flow. However, the microstructural details how such layering determine the anisotropy of permeability are complex and still not well constrained (e.g., Loucks et al. 2012). Microstructural attributes responsible for fluid flow properties are e.g., preferred grain orientations and microcracks responsible for the inter- and intragranular porosity distribution.

✉ Agnes Kontny
agnes.kontny@kit.edu

¹ Institute of Applied Geosciences, Structural Geology and Tectonics, Karlsruhe Institute of Technology, Karlsruhe, Germany

² Gubkin Russian State University of Oil and Gas, Moscow, Russia

Matrix-related porosity in siliciclastic rocks includes three basic types, namely, interpores between grains and crystals, intrapores within minerals, and organic matter pores (e.g., Loucks et al. 2012). The size of pores ranges from sub-capillary (< 0.002 mm) to super-capillary (> 0.5 mm). Generally, the pore space is strongly affected by porosity reduction due to mechanical compaction and cementation processes (e.g., Busch et al. 2022a).

Pfleiderer and Halls (1990) have developed a rapid and efficient magnetic method, where pore space geometry has been determined using the anisotropy of the magnetic susceptibility (AMS) of rocks impregnated with a ferrofluid. Empirical studies suggested that this magnetic pore fabric is related to the pore shape and orientation, and approximates permeability anisotropy (e.g., Pfleiderer and Halls 1990; Robion et al. 2014; Parés et al. 2016). Since AMS is expressed by a second rank tensor, a magnetic anisotropy ellipsoid can be constructed, in which the major, intermediate and minor axes represent the principal anisotropy directions. The ferrofluid is a suspension of magnetite nanoparticles in a carrier fluid (water or oil), and due to the high magnetic susceptibility of isotropic magnetite particles, the AMS of a pore filled with the ferrofluid reflects the pore-network geometry with long versus short principal AMS axes. But the interpretation that magnetic pore fabrics reflect a shape anisotropy of magnetite entering the pores is only true under the assumption that the entire pore is filled homogeneously by a ferrofluid of constant susceptibility. Recent numerical and experimental studies on magnetic pore fabrics by Biedermann (2019) and Biedermann et al. (2021) indicated that shape anisotropy of magnetite alone cannot explain their results, and distribution anisotropy caused by magnetostatic interaction between close magnetite particles have to be considered as well. A further complication is the frequency dependent magnetic susceptibility effect of the ferrofluid as the magnetite grain sizes are in the superparamagnetic range and ferrofluid susceptibility before impregnation has to be known for modeling purposes, because a strong discrepancy between measured and calculated anisotropy degree was found by Biedermann et al. (2021).

Since the introduction of the magnetic pore fabric method in the 1990s, several studies have been performed in order to unravel limiting factors for this method and to better understand the pore fabric geometry of the investigated rocks (e.g., Pfleiderer and Halls 1994; Hrouda et al. 2000; Robion et al. 2014; Parés et al. 2016). One of those factors is the size of the magnetite nanoparticles in the ferrofluid, which is 10 nm according to the specification of the supplier FerroTec. Pfleiderer and Halls (1990) have studied the size of ferrofluid EMG705 by transmission electron microscopy and give a grain size range from 2 to 15 nm with the most common sizes between 6 and 10 nm. Therefore, the ferrofluid can only enter pores with pore throat sizes larger

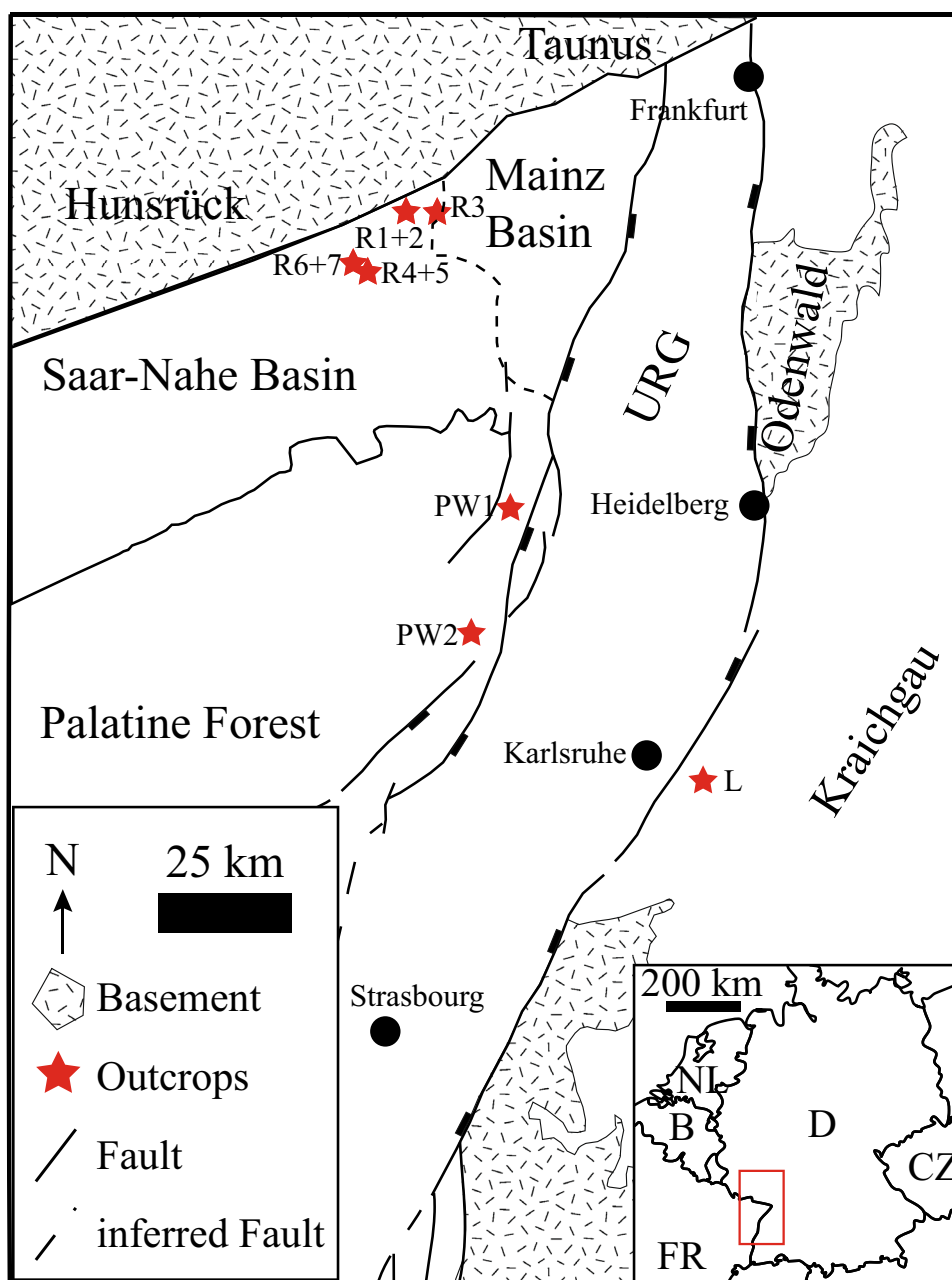
than this size. As the ferrofluid cannot access all the porosity in a rock, Robion et al. (2014) suggested a combination with acoustic anisotropy measurements. Other petrophysical standard methods for the determination of porosity are He- and Hg-porosimetry (via mercury injection capillary pressure (MICP) analyses). Due to the smaller atomic radius He will permeate into small pores with a pore throat radius above ~ 0.06 nm, whereas Hg will permeate into pores with a pore throat radius above ~ 3.5 nm (Busch et al. 2017). He-porosimetry will thus give the highest pore volumes. Consequently, the ferrofluid method will also be limited by the particle size of magnetite nanoparticles and the molecule size of the fluid medium. While He-porosimetry is a non-destructive method (Bohnsack et al. 2021), Hg and ferrofluid porosity determinations will stain the sample and thus measurements may not be reproduced, as the samples are irreversibly altered. However, knowledge of the preferred orientation of pore spaces from susceptibility measurements of ferrofluid impregnated specimens may be an added value to reservoir characterization.

In this study, we used the magnetic susceptibility and its anisotropy for the characterization of the 3D pore space geometry of sandstones from the Permian (Lower and Upper Rotliegend) and the Triassic (Lower and Upper Buntsandstein) of SW-Germany with different porosities and permeabilities. These lithologies are important hydrocarbon and geothermal reservoirs in Germany and NW-Europe (Geluk et al. 2018), and are in the focus of geothermal and hydrocarbon exploration and production in the Upper Rhine Graben (Frey et al. 2022). The aim was to compare the ferrofluid with He-porosity and permeability in order to evaluate the ferrofluid impregnation efficiency, and to determine the orientation, shape and long axis of the pores in relation to the unimpregnated specimen in geographic coordinates. For this purpose, we impregnated the sandstones with an oil- and water-based ferrofluid suspension. These studies were combined with sediment petrographic investigations and the distribution of void space using X-ray micro-computer tomography in order to characterize the sandstones and their microstructural porosity distribution in 2D and 3D. This case study is a new approach of reservoir characterization in sandstones.

Sampling and geological setting of sandstones in SW Germany

Oriented sandstone samples for this study were collected at seven outcrops from the Upper and Lower Rotliegend of the Saar–Nahe Basin, from the Lower Buntsandstein at the western graben shoulder, and from the Upper Buntsandstein of the region around Karlsruhe on the eastern graben shoulder of the Upper Rhine Graben (Fig. 1 and Table 1).

Fig. 1 Simplified geological map of SW-Germany with sample outcrops of the Permo-Triassic sandstones investigated in this study (URG: Upper Rhine Graben; redrawn after Schumacher (2002))



The Saar–Nahe Basin is a late orogenic intermontane basin formed during the Carboniferous and Permian in the late stages of the Variscan orogeny (Stollhofen 2007). It formed as a halfgraben, bound by the Hunsrück Boundary Fault and was filled by ca. 8.5 km of alluvial fan, fluvial, and lacustrine deposits from the Carboniferous Westphalian to the Permian Rotliegend (Henk 1993). The Carboniferous deposits were formed as an initial proto-rift sequence and a prevolcanic syn-rift sequence (Stollhofen 2007). Deposits of the Lower Rotliegend Glan Subgroup (Gzhelian to Asselian) still formed during the prevolcanic syn-rift sequence (Stollhofen 2007; Deutsche Stratigraphische Kommission 2016). Upper Rotliegend sediments of the Nahe Subgroup

(Sakmarian to Kungurian) were deposited in a volcanic syn-rift sequence and a post-rift sequence (Stollhofen 2007; Deutsche Stratigraphische Kommission 2016).

Predominantly fluvial deposits formed during the Triassic Lower Buntsandstein (Induan to Olenekian) (Deutsche Stratigraphische Kommission 2016) in a semi-arid to arid continental environment at the south-western margin of the Germanic Basin, and were mostly sourced from the Gallic-Armorian Massif in France and London Brabant Massif to the west in Belgium (Bourquin et al. 2006). Braided rivers, fringed by alluvial, lacustrine, and aeolian environments are the main depositional systems (Backhaus 1974; Dachroth 1985; Bourquin et al. 2011) overall feeding into a central

Table 1 Lithostratigraphic units and sample locations from the sandstones

Period	Lithostratigraphic unit	Subgroup	Sample number and location	Geographic coordinates	
Trias	Upper Buntsandstein	Plattensandstein	UB_L1, _L2, _L3	N 48.988535	
		(Early Anisian)	(Lerchenberg quarry, Karlsruhe)	E 8.484718	
	Lower Buntsandstein	Rehberg	LB_2	N 49.182696	
		(Olenekian)	(Rehberg near Bindersbach)	E 7.965433	
		Trifels	LB_1	N 49.376011	
	(Induan)	(Gerberberg Quarry near Lindenberg)	E 8.092302		
Perm	Upper Rotliegend	Nahe	UR_R1, UR_R2	N 49.906982	
		(Sakmarian to Kungurian)	(Schützenhaus Windesheim)	E 7.825849	
			UR_R3	N 49.887055	
			(Felseneremitage)	E 7.866822	
	Lower Rotliegend	Glan		LR_R4, LR_R5	N 49.778512
				(roadcut between Duchroth and Odernheim)	E 7.721577
				LR_R6, LR_R7	N 49.7810771
			(Staudernheimer slope, E of Bad Sobernheim)	E 7.6858210	

playa lake in the northern part of the Germanic Basin (Bourquin et al. 2006). During the Upper Buntsandstein a marine incursion into the Germanic Basin (Aigner and Bachmann 1992; Feist-Burkhardt et al. 2008) initiated the transition to marine conditions of the Muschelkalk (Early Anisian to Early Ladinian) (Deutsche Stratigraphische Kommission 2016)).

The Upper Rhine Graben is a NNE-SSW trending, approximately 300 km long and 30–50 km wide rift basin formed as part of the European Cenozoic Rift System (Fig. 1). It separates the Lower Triassic Buntsandstein at the western graben shoulder from the Upper Triassic Buntsandstein at the eastern graben shoulder (Ziegler 1992).

Methods

From the geographically oriented hand samples 5–10 cylindrical specimens of 2.5 cm diameter and 2.1 cm length were drilled perpendicular and some also parallel to the bedding plane for He and ferrofluid porosity, permeability and magnetic susceptibility measurements. In addition, we drilled two cylindrical specimens with a diameter of 1 cm for X-ray micro-computer tomography (X-ray μ CT).

A total of 41 thin sections (of which 16 were polished for reflected light analyses), impregnated with blue-dyed epoxy resin, were prepared for 2D sediment petrography, point counting, and image analyses. For transmitted light and point counting (300 counts) a Leitz Aristomet microscope with a semi-automated Pelcon point counter was used, and for reflected light a Leitz Orthoplan polarizing microscope. Thin sections were oriented parallel to the magnetic foliation (K_{max}–K_{int} section) and perpendicular to magnetic foliation and parallel to magnetic lineation (K_{min}–K_{max}

section). Samples prepared perpendicular to the magnetic foliation were used for point-counting analyses, with a step length adjusted to the maximum grain size to gain area-weighted results (Busch et al. 2020). Normalized quartz, feldspar and rock fragment (QFR) ternary diagrams (Folk 1980) were used to show the analyzed sample composition. The intergranular volume (IGV) was calculated according to Paxton (2002) as the sum of intergranular porosity, intergranular cements, and depositional matrix. Cementational and compactional porosity loss was calculated according to Lundegard (1992). Grain sizes were measured as the long axes of detrital grains on a grid with a step-length adjusted to the maximum observed grain size to gain area-weighted results (Taylor et al. 2022).

ImageJ was used to produce binary images from transmitted light and to determine the percentage of pores and pore orientations (Schneider et al. 2012). During color segmentation of the blue-dyed epoxy resin, only pores > 10 μ m were selected for orientation analysis from which the angle to the vertical edge of the thin section is shown in a histogram. Furthermore, reflected light microscopy of samples embedded in epoxy resin before and after ferrofluid impregnation was used to identify opaque phases, to possibly gain insight into the distribution of ferrofluid in the samples.

Porosity measured by He or Hg injection is a bulk, non-oriented property, whereas permeability depends on the measurement axis. Air permeability was measured under steady state conditions at a constant confining pressure of 1.2 MPa using a Westphal air permeameter along the specimen long axis (Busch et al. 2022b). From the measured flow rate (ml/min), the pressure gradient across the specimen, gas viscosity, and specimen dimensions, the permeability was calculated according Darcy's law and recalculated into Klinkenberg-corrected permeability according to

Rieckmann (1970). The used equipment has a measurement range of 0.0001 to 10,000 mD ($1 \cdot 10^{-19}$ to $1 \cdot 10^{-11}$ m²). The measured air permeability values are a function of the connected porosity and pore throat sizes. As we measured only this one type of permeability, we use in the following only the term permeability.

Helium porosity (a measure of connected porosity) and sample densities were measured with a Micromeritics AccuPyc II 1340 gas pycnometer (sensitivity of 0.045 cm³) (Becker et al. 2019). Using Boyle’s law, the solid volume of a specimen can be determined. Subtracting this volume from the bulk cylinder volume gives the pore volume of the specimen, and its relation to the bulk cylinder volume gives the porosity. Isolated porosity, not contributing to fluid flow through the specimen, is therefore not measured by this procedure.

Mercury intrusion porosimetry was performed for one sample from each outcrop using a porosimeter from Micromeritics, type AutoPore IV 9520 (pore throat size 360–0.003 μm; pressure 410 MPa) at the Institute of Applied Geosciences, KIT. This method permits the calculation of the pore throat size distribution within the sample and allows an evaluation of the percentage of pores greater than 10 nm that can be impregnated by the ferrofluid (Knopp et al. 2022).

The ferrofluid porosity (Φ_{ff}) was obtained by the following relationship after Pfeleiderer (1992):

$$\Phi_{ff} = (msatff - mdry) / \rho_{ff} * V \tag{1}$$

where Φ_{ff} is the ferrofluid porosity, msatff is the mass of the specimen after impregnation with ferrofluid, mdry is the mass of the specimen before impregnation drying for approx. 24 h at 40 °C in a vacuum oven, V is the specimen volume and ρ_{ff} is the density of the ferrofluid.

For ferrofluid impregnation we used two different ferrofluids, water-based EMG807 and oil-based EMG905 from FerroTec. We used different dilution for the water- and oil-based ferrofluid to avoid problems with the upper measuring range of the KLY-4S Kappabridge (0.2 SI). Table 2 shows petrophysical properties and magnetic susceptibility from the manufacturer and the diluted values measured with the

Kappabridge. The dilution of 1:10 and 1:30 corresponds to a difference in magnetic susceptibility of about 14, which cannot be explained by the dilution difference but likely is related to different frequencies at which the measurements from FerroTec and us are performed. According to Biedermann et al. (2021) the effective susceptibility of the ferrofluid depends on the measurement frequency.

The specimens were dried in a vacuum oven and weighed before impregnation. Then they were placed in a dish, which was filled with the ferrofluid and completely covered the specimen at the beginning of the impregnation process. The tray with specimens was then placed in a desiccator. A vacuum of 10 mbar (0.001 MPa) was set in the desiccator for approximately 72 h. During this period, the specimens were turned over several times in the ferrofluid. Due to the lower proportion of ferrofluid in the oil-based mixture and the volatilization of the oil, the injection tray had to be refilled several times during injection. The specimens were then removed from the dish and weighed individually. This protocol is similar to those described earlier by Robion et al. (2014) and Parés et al. (2016, see Fig. 3 therein) with slight modifications concerning the ferrofluid type and the dwell time in the desiccator. The nominal magnetite particle diameter in both ferrofluid types is 10 nm (FerroTec).

We also calculated the mass and susceptibility impregnation efficiency (I.E.mass and I.E.susc) after Pugnetti et al. (2022). Mass impregnation efficiency is the above given formula for the ferrofluid porosity modified by considering the porosity (por) in the denominator:

$$I.E._{mass} = (msatff - mdry) / (por * \rho_{ff} * V) * 100(\%),$$

and susceptibility impregnation efficiency is defined as:

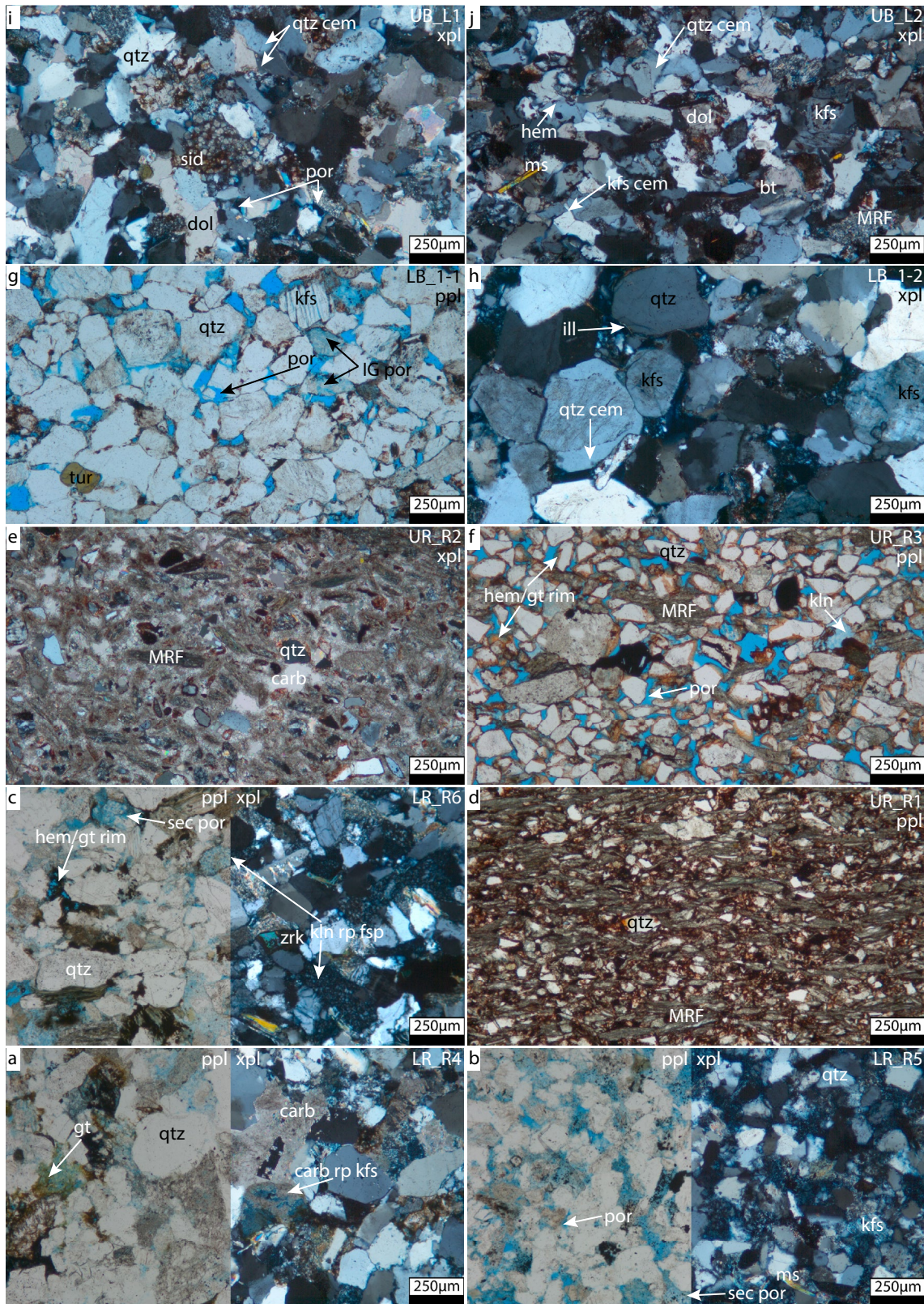
$$I.E._{susc} = (Ksatff - Kdry) / (por * K_{fluid}) * 100(\%),$$

where Ksatff and Kdry are the volume-normalized magnetic susceptibility of the impregnated and unimpregnated specimen, respectively, and K_{fluid} is the effective susceptibility of the fluid measured with the Kappabridge (Table 2).

The anisotropy of low field magnetic susceptibility (AMS) was measured with a fully automated KLY-4S

Table 2 Intrinsic physical properties of the ferrofluid given by the manufacturer FerroTec and magnetic susceptibility measured in diluted quantity by the KLY-4S Kappabridge in a field of 300 A/m and a frequency of 875 Hz

Ferrofluid	Density	Viscosity@27 °C	Saturation magnetization	Magnetic susceptibility		
	FerroTec	FerroTec	FerroTec	FerroTec	KLY-4S 1:10	KLY-4S 1:30
EMG807 (water)	1.1 g/cm ³	<5 mPa s	11 mT	1.88 SI	6.62*10 ⁻⁶ m ³ /kg	
EMG905 (oil)	1.2 g/cm ³	<5 mPa s	44 mT	3.52 SI	96.85*10 ⁻⁶ m ³ /kg	



Kappabridge (AGICO, Czech Republic) in a field of 300 A/m and a frequency of 875 Hz. The operator has to adjust the specimen only in three perpendicular positions and one

specimen is measured in about 3 min. The sensitivity of the instrument is 3×10^{-8} SI units for specimens of a volume of 10 cm^3 (Pokorny 2004), and the anisotropy is also

Fig. 2 Sediment petrography of sandstones from Rotliegend and Buntsandstein facies of SW-Germany. Subarkose: **a** LR_R4 (left: ppl and right: xpl); feldspathic litharenite **(b)** LR_R5 (left: ppl and right: xpl); sublitharenite **(c)** (LR_R6, ppl and xpl); litharenite: **d** UR_R1 (ppl), **(e)** UR_R2 (xpl), **(f)** UR_R3 (ppl); subarkose **(g)** LB_1-1 (ppl) and **(h)** LB_1-2 (xpl); lithic arkose **(i)** UB_L1 and **(j)** UB_L2 (xpl), *bt* biotite, *carb* carbonate, *cem* cement, *dol* dolomite, *gt* goethite, *hem* hematite, *kfs* kalifeldspar, *kln* kaolinite, *MRF* metamorphic rock fragment, *ms* muscovite, *por* pore, *qtz* quartz, *rp* replaces, *sid* siderite, *tur* tourmaline, *zrk* zircon, *ppl* plane polarized light, *xpl* crossed polarized light. Thin sections are impregnated with blue dyed resin

very precise due to a total of 192 measurements for each specimen.

Principal susceptibility axes with $K_{max} > K_{int} > K_{min}$ were calculated using the program SUFAR and the mean bulk susceptibility K_{mean} , the eccentricity P , and the shape factor T of the AMS ellipsoid were computed according to $K_{mean} = (K_{max} + K_{int} + K_{min})/3$, $P = K_{max}/K_{min}$, and $T = 2\ln(K_{int}/K_{min})/\ln(K_{max}/K_{min}) - 1$. AMS measured in the SUFAR mode considers a demagnetization factor as the shape of the AMS in strong ferrimagnetic specimens due to magnetite is biased by a self-demagnetization effect (e.g., Uyeda et al. 1963; Hrouda et al. 2000). In magnetic pore fabric studies the self-demagnetization effect results in a shape anisotropy if the pores are non-spherical (Biedermann 2019), and reflects the preferred orientation of ferrofluid-filled pores (Hrouda et al. 2000). Self-demagnetization becomes important for susceptibilities of > 0.1 SI and can play a role in magnetic pore fabric studies even if the ferrofluid is diluted (Biedermann 2019).

In addition to ferrofluid porosity, we determined the anisotropy of the magnetic ferrofluid susceptibility (AMFFS) of the impregnated specimen. In order not to contaminate the Kappabridge during the measurement of AMFFS with ferrofluid, the specimens were wrapped in thin transparent film and sealed with adhesive tape (supplementary material 1). AMFFS measurement was then performed in the Kappabridge. The magnetic susceptibility of the clear film is $3.78 \cdot 10^{-8}$, which is in the range of the sensitivity of the instrument. Therefore, the very low value of the clear film in relation to the specimen was neglected in the following. AMFFS (also called magnetic pore fabric) measurements were conducted within a few days after ferrofluid impregnation to avoid artefacts that may arise from changes in ferrofluid properties over time (Biedermann and Parés 2022; Pugnetti et al. 2022). Magnetic susceptibility of the rock specimen is one to four orders lower than the impregnated specimen. Therefore, we classified the original AMS as insignificant for the AMFFS and have not subtracted the original AMS from the AMFFS. Biedermann and Parés (2022) have described a 2.5–3 times increase of magnetic susceptibility after 4 years in rocks impregnated with oil-based ferrofluid. They speculated that the oil may have

reduced some of the hematite into magnetite in the red sandstones. In such a case or if the rock aimed for magnetic pore fabric studies shows already a ferrimagnetic susceptibility, the tensorial sum of the natural (non-impregnated) rock AMS must be subtracted from AMFFS.

Results

Detrital components and authigenic phases

Detrital and authigenic compositions of the studied sandstones vary between the different stratigraphic levels and outcrops (see supplementary material 2). The main differences, with influence on the magnetic susceptibility is briefly described below.

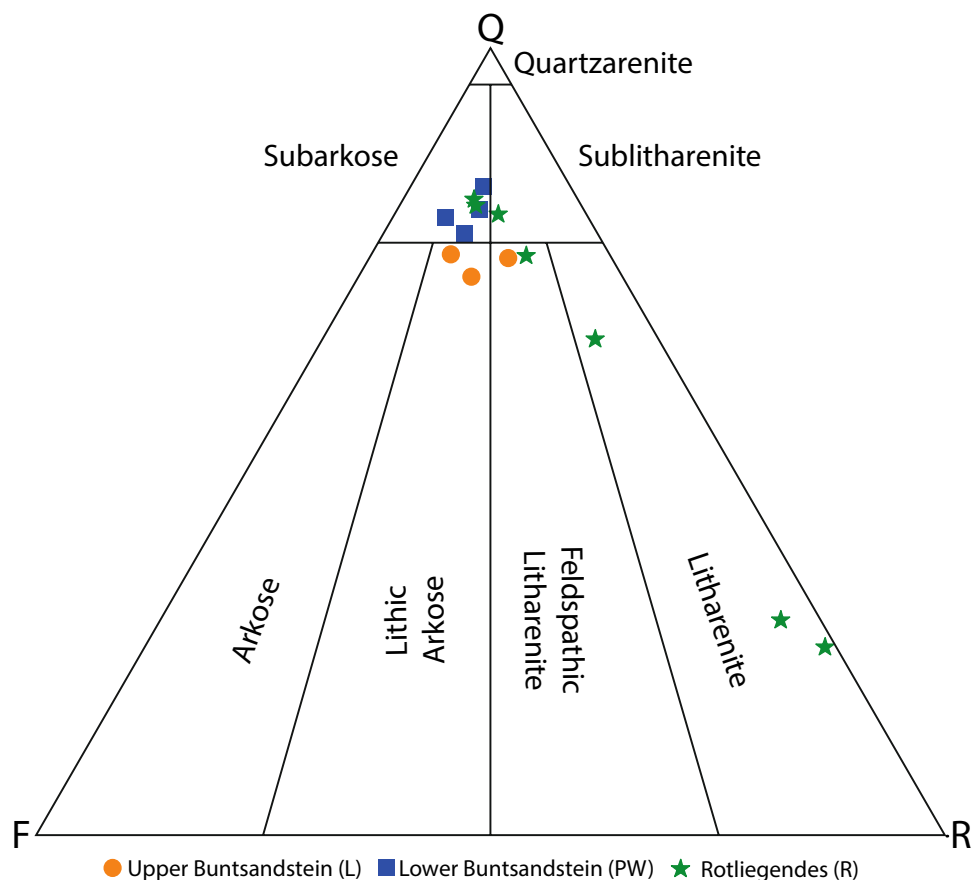
Sandstones from the Lower Rotliegend (LR_R4 to LR_R7) contain a relative high quartz content (52–59%, Fig. 2a–c) and low amount of rock fragments (5–12%, including sedimentary, igneous, and metamorphic rocks, Fig. 2a–c), and can be classified as subarkoses, sublitharenites, and feldspathic litharenites. Detrital micas range from 1 to 2.7%. The most prominent authigenic phases are dolomite and siderite (0–7%), illite (1–5%), hematite and goethite (1–3%, Fig. 2a, b), kaolinite (3–9%, including kaolinite replacements after K-feldspar, Fig. 2a, c).

Sandstones from the Upper Rotliegend (UR_R1 to UR_R3) contain low contents of detrital quartz grains (17–47%, Fig. 2d–f), whereas rock fragments are more prominent (22–54%, including sedimentary, igneous, and metamorphic rocks, Fig. 2d, e), and all classify as litharenites (Fig. 3). Detrital micas comprise 0.3 to 3% of the studied samples. Furthermore, samples UR_R1 and UR_R2 contain mm-thick shale laminae composed of Fe-rich detrital clay (2–16%). The most prominent authigenic phases include dolomite and siderite (1–19%), kaolinite (0–2%, including kaolinite replacements after K-feldspar), and hematite and goethite (1–3%, Fig. 2d, f).

Sandstones from the Lower and Upper Buntsandstein (LB and UB) are quartz-rich (41–66% Fig. 2g–j), contain the highest amounts of feldspar grains (7–12%, Fig. 2g, j), and can be classified as subarkoses, lithic arkoses, and feldspathic litharenites (Fig. 3). Detrital micas are less prominent in the LB samples ($< 0.7\%$, Fig. 2g, h) compared to those from the UB samples (0.7 to 2.3%, Fig. 2i, j). Sandstones from the Lower Buntsandstein are devoid of any carbonate cements, whereas samples from the Upper Buntsandstein contain 1–23% dolomite and siderite. Both sample series contain 0.3 to 4% hematite and goethite, 0–2% illite, and 0–1% kaolinite (including kaolinite replacements after K-feldspar).

All sandstones are composed of fine to medium sized particles in the range of 0.08 to 0.3 mm. Under reflected

Fig. 3 QFR composition of the studied sandstones (plotted after Folk (1980))



light, only ilmenite and rutile (combined above as TiO_x) as detrital phases and goethite and hematite as pigmented rims, pore fillings, and detrital grains were observed. Magnetite was not observed in any of the sandstones, in agreement with the low magnetic susceptibility (see below). For sample LR_R4 we also performed reflected light microscopy for a water-based ferrofluid-impregnated specimen and found no change in Fe-oxide mineralogy. We were not able to observe the magnetite nanoparticles in conventional reflected light microscopy using a ferrofluid coating of the polished thin section, indicating no significant agglomeration or reaction with the existing Fe-oxides or clay minerals into magnetite. However, we cannot exclude the possibility that during polished thin section preparation using epoxy resin the ferrofluid impregnation disappeared. This aspect needs further investigations.

Porosity and permeability

The investigated sandstones from SW-Germany show a large range of He porosities (2–26%) and permeabilities (0.002–1800 mD) with regional and stratigraphic differences (Fig. 4a). While sandstones from the Lower Buntsandstein of the Palatine Forest (LB) show relatively high porosities between 12 and 26% and permeabilities between

0.2 and 1800 mD, sandstones from the Upper Buntsandstein of the eastern Upper Rhine Graben shoulder (UB) show relatively low porosities between 2 and 16% and permeabilities between 0.01 and 0.09 mD, with only one exception (85 mD, Fig. 4a). A positive correlation exists between these two petrophysical parameters, which is better defined at low porosities/permeabilities, while a larger variation in permeabilities is observed for specimens with porosities > 15%.

For some samples from Upper Buntsandstein (L1–L3) and Rotliegend (R2–R7) sandstones permeability was additionally measured parallel and perpendicular to bedding. Permeability parallel to bedding is higher or equal compared to the permeability measured perpendicular to bedding independent of permeability and He porosity (Fig. 4b).

Porosity and permeability are closely related to grain size, the cementational porosity loss, and the intergranular volume (Supplementary Material 3). Porosity and permeability increase with larger detrital grain sizes, and decrease with higher cementational porosity loss and higher intergranular volume.

The pore throat diameter determined by Hg porosimetry ranges from 0.08 to 34.5 μm in Rotliegend sandstone (0.95–34.5 μm in Lower Rotliegend, and 0.08 to 12.16 μm in Upper Rotliegend), and more than 98% of the pores could be impregnated by the ferrofluid, except in specimens

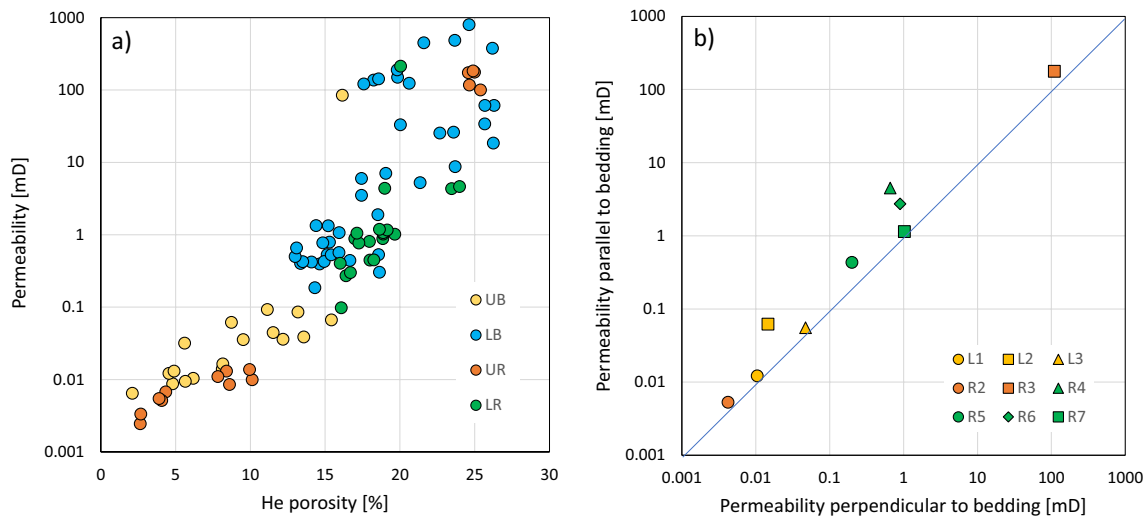


Fig. 4 **a** Permeability as function of He porosity for sandstones from the Lower (LR) and Upper (UR) Rotliegend from the Saar-Nahe Basin and the Lower (LB) and Upper (UB) Buntsandstein of

R1 and R2 where only 92% and 86%, respectively, of the pores can be impregnated by ferrofluid. In sandstone from Lower Buntsandstein pore throat diameters range from 21 to 77 μm , and in sandstones from the Upper Buntsandstein pore throat diameters are significantly smaller and range from 0.6 to 1.2 μm . The pores can be classified as sub-capillary micropores as all diameters are below 0.4 mm (e.g., Nabawy et al. 2009). The data show that more than 96% of the pore volume is connected by pore throats > 10 nm allowing an injection by the ferrofluid.

Susceptibility and efficiency of ferrofluid impregnation

Magnetic susceptibility of the unimpregnated sandstones from the Lower Buntsandstein are lowest with an average of $19 \cdot 10^{-6}$ SI, sandstones from Upper Buntsandstein and Lower Rotliegend are intermediate with average values of $54 \cdot 10^{-6}$ SI, and specimens from the Upper Rotliegend are highest with an average of $238 \cdot 10^{-6}$ SI (Tables 3, 4), indicating the highest amount of paramagnetic minerals. This data agrees with the higher amount of phyllosilicate-rich metamorphic rock fragments in the sedimentary rocks from the Upper Rotliegend (Fig. 2d, e). Magnetic susceptibility after impregnation correlates with the mass of the injected ferrofluid, but magnetic susceptibility values are much higher in the specimens impregnated with oil-based ferrofluid (up to $270 \cdot 10^{-3}$ SI) than in those impregnated with water-based ferrofluid (up to $6 \cdot 10^{-3}$ SI). The positive correlation between mass of the ferrofluid and magnetic susceptibility is better in specimens impregnated with the oil-based ferrofluid

the western and eastern Rhine Graben shoulder near Landau and Karlsruhe, respectively. **b** Comparison of permeability for specimen prepared parallel and perpendicular to bedding

($R^2 = 0.926$ in oil-based ferrofluid and $R^2 = 0.6743$ in water-based ferrofluid, Fig. 5a).

In order to test the efficiency of ferrofluid impregnation we compared the calculated ferrofluid porosity with measured He porosity. For both impregnation methods we observed a positive correlation between ferrofluid and He porosity (Fig. 5b) with correlation coefficients of $R^2 = 0.933$ for oil-based and $R^2 = 0.934$ for water-based ferrofluid. These results imply that the greater the He porosity, the more ferrofluid can be injected and the higher is the magnetic susceptibility. The mean deviation between helium porosity and ferrofluid porosity is 7% for oil-based (5% if specimens with I.E.mass $< 58\%$ were omitted, Table 3), and 3% for water-based ferrofluid impregnation with He porosity for all specimens always higher or equal to ferrofluid porosity. But again, there is a clear difference between the sandstones of the different areas (Table 3). The lowest scatter is observed in specimen from the Rotliegend ($< 1 - 3.8\%$), and the highest scatter in those from the Lower Buntsandstein (1–15%). In sandstones from the Upper Buntsandstein the range of porosity deviation is 2 to 9%.

Comparing the magnetic susceptibility with He porosity and permeability, we also noted a better correlation of specimens impregnated with oil-based ferrofluid (Fig. 5c, d). These results imply a better impregnation efficiency for the oil-based compared to the water-based ferrofluid, and likely suggest that specimens were not completely saturated by the ferrofluid.

Our data show no correlation between the difference of the two used porosity methods and permeability. Therefore, the difference does not seem to be related to low permeabilities that prevent infiltration of the ferrofluid. The

Table 3 Magnetic susceptibility, permeability and porosity data for single unimpregnated and then impregnated sandstone specimens

Sample	V		mass		Unimpregnated (AMS)		T		mass FF		Impregnated (AMFFS)						
			K	P	K	P			K	P	T	Perm	He por	FF por	Diff	I.E.mass	I.E.susc
Water-based ferrofluid EMG807																	
UB_L1-12-1S	10.76	27.49	3.43E-05	1.03	-0.41	0.32	3.54E-04	1.12	0.84	0.01	4.54	2.92	1.62	58.95	0.37		
UB_L2-3-2S	10.91	27.88	5.81E-05	1.07	0.66	0.20	3.40E-04	1.05	0.13	0.01	4.88	1.81	3.07	33.97	0.31		
UB_L3-1-2S	10.76	25.22	7.24E-05	1.06	0.80	1.17	2.59E-04	1.05	-0.50	0.04	15.41	10.74	4.67	63.93	0.06		
LB_1-1-1-2	10.68	24.49	1.34E-05	1.05	0.41	1.07	2.13E-03	1.02	0.43	0.40	14.62	9.95	4.67	62.44	0.77		
LB_1-1-3-2	10.76	24.41	1.96E-05	1.05	0.83	1.37	3.89E-04	1.10	-0.67	0.43	14.92	12.62	2.31	77.55	0.13		
LB_1-2-3-2	10.76	23.59	8.16E-06	1.06	0.07	1.63	4.47E-03	1.02	0.76	138.11	18.23	15.02	3.21	75.58	1.30		
LB_1-2-12-3	10.62	23.88	1.34E-05	1.06	-0.28	1.27	2.68E-04	1.07	-0.58	1.34	15.20	11.86	3.34	71.56	0.09		
LB_2-1-9-1	10.76	22.18	1.45E-05	1.03	0.38	1.78	5.16E-03	1.03	0.31	8.79	23.68	16.35	7.34	63.31	1.16		
LB_2-2-6-1	10.76	24.86	4.64E-05	1.08	0.49	1.13	1.93E-03	1.02	0.33	0.19	14.30	10.41	3.89	66.75	0.70		
LB_2-2-18-1	10.76	24.49	2.79E-05	1.07	0.57	1.46	3.93E-04	1.08	0.38	1.35	14.38	13.46	0.92	85.86	0.13		
UR_R1-1-1	10.31	25.67	2.53E-04	1.13	0.90	1.05	2.23E-03	1.08	-0.31	0.00	10.11	10.07	0.04	91.38	1.04		
UR_R2-2-2S	10.55	28.32	2.34E-04	1.09	0.94	0.20	2.04E-03	1.04	-0.65	0.00	2.63	1.92	0.70	67.16	3.66		
UR_R3-7-1P	10.75	21.92	2.21E-04	1.35	0.87	2.30	5.82E-03	1.05	-0.54	177.06	24.98	21.22	3.76	77.94	1.19		
LR_R4-3-1S	10.70	23.43	4.33E-05	1.01	0.00	1.79	3.02E-03	1.06	-0.57	0.89	18.85	16.59	2.26	80.73	0.84		
LR_R5-8-1P	10.89	23.96	5.08E-05	1.01	0.34	1.65	3.13E-03	1.15	0.52	0.45	17.99	15.00	2.99	76.51	0.91		
LR_R6-3-2S	10.84	23.54	5.57E-05	1.03	0.92	1.73	2.48E-03	1.12	0.56	1.03	18.87	15.81	3.06	76.86	0.68		
LR_R7-6-1P	10.79	23.53	6.28E-05	1.03	0.66	1.76	3.11E-03	1.03	0.30	1.08	18.87	16.12	2.75	78.38	0.86		
Oil-based ferrofluid EMG905																	
UB_L1-1-1S	10.62	27.07	3.19E-05	1.03	-0.30	0.19	1.25E-02	1.19	0.78	0.01	4.79	1.79	3.00	31.46	7.41		
UB_L2-6-4S	10.76	26.63	5.59E-05	1.06	0.35	0.30	1.72E-02	1.10	0.42	0.02	8.14	2.73	5.40	28.26	5.98		
UB_L3-2-2S	10.71	25.48	7.52E-05	1.05	0.64	0.56	3.33E-02	1.49	0.53	0.04	12.17	5.14	7.03	35.54	7.75		
LB_1-1-4-1	10.86	24.35	1.15E-05	1.05	0.23	1.18	1.09E-01	1.04	0.45	0.53	15.40	10.77	4.63	58.82	20.11		
LB_1-1-8-1	10.76	24.62	2.09E-05	1.06	0.58	0.34	3.13E-02	1.07	0.56	0.30	15.12	3.13	11.99	17.41	5.87		
LB_1-2-2-2	10.71	23.41	8.12E-06	1.05	0.06	1.45	1.65E-01	1.03	0.38	122.11	17.57	13.39	4.19	64.05	26.61		
LB_1-2-8-1	10.81	23.27	7.16E-06	1.05	-0.25	0.85	4.21E-02	1.05	0.43	190.72	19.80	7.79	12.01	33.09	6.04		
LB_2-1-12-1	10.76	21.45	1.78E-05	1.05	0.62	1.02	4.81E-02	1.09	0.22	18.62	26.23	9.39	16.84	30.11	5.20		
LB_2-1-18-1	10.86	21.38	2.66E-05	1.06	0.53	2.13	2.18E-01	1.02	0.74	380.20	26.17	19.47	6.70	62.57	23.65		
LB_2-2-2-1	10.76	24.16	3.85E-05	1.07	0.56	0.36	1.94E-02	1.10	0.46	0.45	16.64	3.32	13.33	16.75	3.30		
LB_2-2-27-2	10.81	22.18	1.40E-05	1.07	0.64	1.92	2.02E-01	1.02	0.07	25.53	22.66	17.60	5.06	65.31	25.31		
UR_R1-3-2	10.75	27.28	2.67E-04	1.14	0.91	0.66	2.03E-02	1.48	0.85	0.01	8.40	6.04	2.36	60.48	6.77		
UR_R2-10-3P	10.46	27.83	2.35E-04	1.10	0.96	0.29	8.91E-03	1.16	-0.35	0.01	3.88	2.80	1.09	60.55	6.34		
UR_R3-7-2P	10.70	21.92	2.19E-04	1.36	0.87	2.04	2.62E-01	1.08	0.86	174.46	24.56	18.86	5.70	64.58	30.23		

Table 3 (continued)

Sample	V		mass		Unimpregnated (AMS)		T		mass FF		Impregnated (AMFFS)							
					K	P					K	P	T	Perm	He por	FF por	Diff	I.E.mass
LR_R4-7-2P	10.70	22.10	4.37E-05	1.01	0.39	1.01	0.39	1.01	1.97	2.40E-01	1.03	0.22	4.35	23.44	18.27	5.17	65.55	29.02
LR_R5-8-2P	10.79	24.37	5.11E-05	1.01	0.31	1.01	0.31	1.23	7.70E-02	1.07	0.15	0.41	15.99	11.32	4.67	59.52	13.67	
LR_R6-7-1P	10.89	23.65	5.83E-05	1.02	0.87	1.02	0.87	1.58	1.68E-01	1.04	0.49	4.42	18.98	14.35	4.63	63.58	25.10	
LR_R7-6-2P	10.84	23.49	6.28E-05	1.03	0.75	1.03	0.75	1.61	1.72E-01	1.07	0.71	1.17	19.14	14.68	4.46	64.49	25.45	

AMS anisotropy of magnetic susceptibility, AMFFS anisotropy of magnetic ferrofluid susceptibility, mass [g], V volume [cm³], K magnetic susceptibility [SI], P degree of anisotropy, T shape factor, FF ferrofluid, Perm permeability [mD], por porosity [%], Diff difference between He and FF porosity [%], I.E.mass impregnation efficiency [%], I.E.susc susceptibility impregnation efficiency [%]

difference between higher He and lower ferrofluid porosity varies from < 1 to 7% in the water-based ferrofluid, and from 1 to 17% in the oil-based ferrofluid (Table 3). We assume that a high percentage of pores other than the very small pores below 10 nm (size of magnetite particles in the ferrofluid) were impregnated by the ferrofluid and the magnetic pore fabric should give reliable results. The four specimens impregnated with oil-based ferrofluid that show the strongest difference (LB_1-1-8-1, LB_1-2-8-1, LB_2-1-12-1 and LB_2-2-2-1) were likely not well enough impregnated.

If the ferrofluid fills the pore space as a homogeneous fluid with constant density and susceptibility, the mass and susceptibility impregnation efficiency determined for the same specimen are expected to be the same (Pugnetti et al. 2022). In our study for sandstones, we observed a significantly larger I.E.mass than I.E.susc (Fig. 6). For specimens impregnated with water-based ferrofluid, mass impregnation efficiency ranges from 34 to 91% and for specimens impregnated with oil-based ferrofluid it ranges from 17 to 78% (Fig. 6a, c). Susceptibility impregnation efficiency for water-based ferrofluid ranges from 0.1 to 3.7%, and for oil-based ferrofluid it is significantly larger and shows a strong variability between 5 and 30% (Fig. 6b, c).

Shape of AMS and AMFFS

We measured the anisotropy of magnetic ferrofluid susceptibility (AMFFS) of the impregnated sandstone specimens to determine the magnetic pore fabric geometry, and compared the ellipsoid shapes and their orientation to the anisotropy of magnetic susceptibility (AMS) of the unimpregnated sandstone.

Shape factor (T) and degree of anisotropy (P) of sandstones from the Lower and Upper Buntsandstein are very similar and range from prolate to oblate shapes (T: – 0.3–0.83) with P values between 1.03 and 1.08 (Table 3). The strong variation of T indicates the existence of two competing magnetic fabric planes (see also Fig. 8). Sandstones from the Lower Rotliegend show even lower P values between 1.01 and 1.03 and oblate shapes (T: 0–0.92). The sandstones from the Upper Rotliegend show the highest magnetic susceptibility compared to all other sandstones and strongest oblate shapes (T: 0.87–0.96) and highest P values between 1.09 and 1.36. These latter data agree well with a relatively high amount of phyllosilicate-rich metamorphic rock fragments aligned parallel to bedding (Fig. 2).

Comparing each specimen before impregnation (black) with the shape after water-based (blue) and oil-based ferrofluid impregnation (orange, Fig. 7) there is not much change in the shape, except that in water-based ferrofluid impregnated specimens five move from the oblate into the prolate field (Fig. 7c, Fig. 8d). These specimens are characterized by inverse fabrics as it is shown in the next chapter (Tables 5, 6

Table 4 Summary of AMS data from unimpregnated sandstone specimens with mean magnetic susceptibility (Kmean) and mean orientation for Kmax, Kint, Kmin

Sam- ples	N	Kmean	std error	P	std error	T	std error	Kmax_ Dec	Kmax_ Inc	Confidence ellipse			Kmin_ Dec	Kmin_ Inc	Confidence ellipse				
										J	B	J			B	J	B		
UB_ L1	19	3.73E-05	8.59E-06	1.026	0.002	-0.101	0.297	97	5	6.2/3.4	3.5/2.1	7	6	10.5/6.1	3.5/6.0	228	83	10.5/3.5	5.9/2.1
UB_ L2	26	5.86E-05	2.58E-06	1.058	0.006	0.575	0.142	116	4	28.7/5.7	15.6/2.9	25	17	28.9/13.7	15.6/7.1	219	73	14.3/5.3	7.1/2.9
UB_ L3	19	7.37E-05	2.46E-06	1.05	0.002	0.706	0.07	293	3	16.7/1.5	9.6/0.9	203	2	16.8/1.3	9.6/1.2	82	87	2.2/1.4	1.2/0.9
LB_1- 1	48	1.39E-05	4.77E-06	1.073	0.023	0.321	0.244	227	6	12.4/7.9	4.4/2.9	317	1	12.2/7.3	4.3/2.7	60	84	8.4/7.1	2.7/2.9
LB_1- 2	28	1.50E-05	1.51E-06	1.06	0.007	0.184	0.21	98	5	6.2/4.0	2.6/2.2	188	0	20.3/5.5	2.6/10.2	279	85	20.4/3.7	10.2/2.3
LB_2- 1	30	1.68E-05	3.66E-06	1.051	0.012	0.566	0.207	258	10	42.7/10.8	23.8/6.3	166	15	42.8/12.5	23.8/6.3	21	72	14.3/9.2	6.2/4.8
LB_2- 2	40	3.47E-05	1.46E-05	1.063	0.01	0.535	0.136	159	4	30.5/11.3	13.4/4.5	69	2	30.6/8.2	13.4/3.7	305	86	12.4/7.2	3.6/4.5
UR_ R1	14	2.64E-04	6.40E-06	1.12	0.003	0.9	0.019	354	3	12.4/3.9	8.0/3.2	264	8	12.2/2.8	8.0/2.2	105	82	4.7/3.2	2.2/3.2
UR_ R2	14	3.47E-04	7.28E-06	1.077	0.01	0.903	0.042	166	2	56.3/3.9	90.0/4.3	256	3	56.3/5.5	90.0/4.4	37	86	6.4/3.2	3.8/3.1
UR_ R3	18	2.16E-04	2.81E-06	1.309	0.015	0.876	0.024	185	3	45.6/7.1	52.3/6.8	276	8	45.5/4.3	52.3/4.8	77	82	13.0/2.5	4.7/6.3
LR_R4	21	4.39E-05	1.75E-06	1.01	0.002	0.258	0.237	100	2	18.5/10.7	8.8/7.9	191	33	16.4/9.6	8.8/5.7	7	58	14.3/9.6	5.6/7.9
LR_R5	18	5.08E-05	2.77E-06	1.012	0.002	0.312	0.329	176	6	18.0/11.3	10.9/6.6	85	13	18.0/6.6	10.8/4.1	290	76	11.4/6.6	4.0/6.6
LR_R6	15	5.60E-05	1.67E-06	1.021	0.002	0.758	0.129	232	5	36/8/6.0	33.3/4.9	141	7	36.7/4.5	33.3/3.5	357	81	7.5/5.2	3.4/4.8
LR_R7	11	6.29E-05	1.91E-06	1.022	0.002	0.727	0.089	282	6	57.9/7.1	90.0/16.1	12	4	58.4/11.5	90.0/15.2	134	83	21.5/7.4	16.3/6.1

J: Jelimek
B: Bootstrap

Confidence ellipse (error angle around the average axis) is calculated with the program Anisoft5

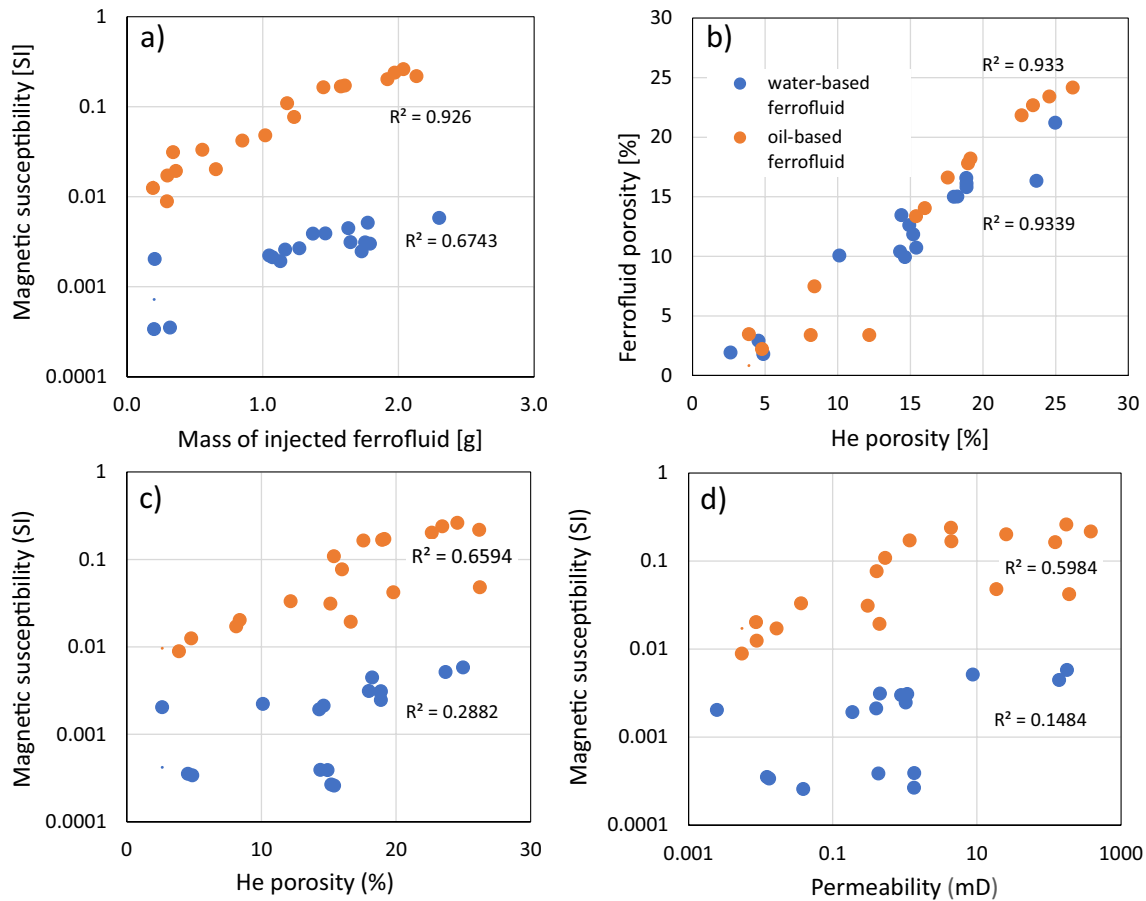


Fig. 5 **a** Magnetic susceptibility versus mass of injected ferrofluid for water- (1:10, blue) and oil-based (1:30, orange) ferrofluid mixtures for sandstones. **b** Comparison of ferrofluid and He porosity. Magnetic

susceptibility (**c**) versus He porosity, and **d** versus permeability. R^2 is coefficient of determination for trend lines

and Fig. 9). In oil-based ferrofluid impregnated specimens (Fig. 8d), no major changes of the ellipsoid geometry occur, which indicates that the ferrofluid strongly impacts the magnetic susceptibility but only little the shape factor.

Orientation of AMS and AMFFS

The orientation of the AMS ellipsoid axes is largely parallel with the depositional bedding of the sandstones with the K_{min} axes (sub-)vertical and K_{max} axes (sub-)horizontal (Fig. 8). Oblate and triaxial fabrics dominate. The clustering of the K_{min} axes shows Jelinek confidence angles corresponding to the ellipsoid principal axes lower than $14^\circ/10^\circ$ for every specimen (Table 4), except for LB_1-2 ($20^\circ/4^\circ$) and LR_R7 ($22^\circ/7^\circ$). However, there are only few specimens (UR_R2 and UB_L3S) that show very well defined vertical K_{min} axes (confidence angles for K_{min} axes below $8^\circ/7^\circ$) and horizontal magnetic foliation, which likely indicate laminated sediment fabrics deposited on a horizontal plane by gravitational forces.

Most sandstone fabrics are slightly tilted indicating hydrodynamic forces, which are typical for fluvial depositional systems with imbricated detrital grains and low angle cross bedding. Variations in the tilt angle likely indicate current velocity changes (e.g., Tarling and Hrouda 1993) and seem to change within individual hand samples (see e.g., UR_R3, LB_1-2, UB_L2S) suggesting small-scale variations of depositional flow conditions, i.e., within an individual fluvial channel. The elongation of the K_{min} axes within one hand sample may indicate an imbrication of detrital grains suggesting current flow directions often oriented towards NNE in the study areas. In hand sample LB_2-2 field observations have shown cross bedding (bedding plane S_0 : $138/13$ and crossbedding plane orientation S_s : $137/27$, given as dip direction and dip), which agrees with the magnetic fabric for the specimens. The K_{max} axes is oriented towards SE (Fig. 8). Therefore, the variation in dip directions of cross beds are reflected by the magnetic fabrics.

Figure 9 shows the magnetic fabrics of single specimens, which are either impregnated with the water-based ferrofluid

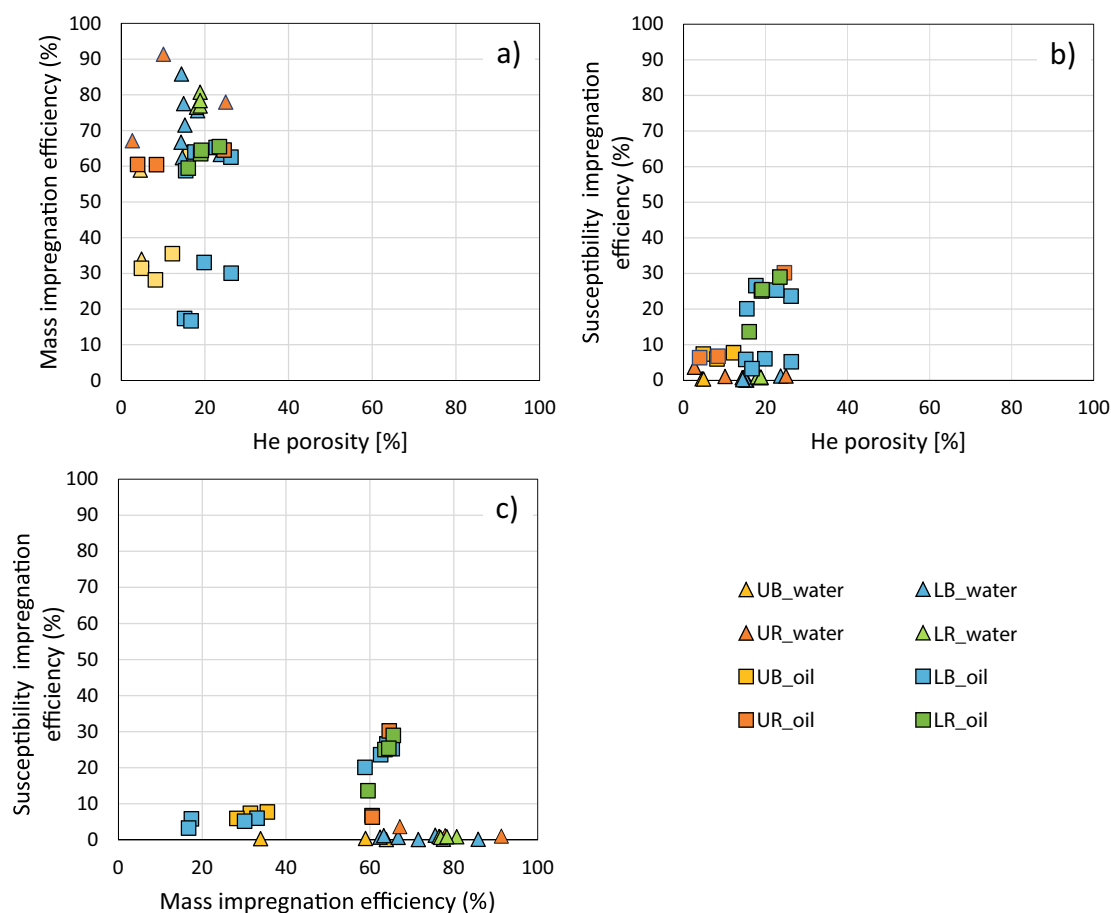


Fig. 6 **a** Mass-based impregnation efficiency versus He porosity. **b** Susceptibility-based impregnation efficiency versus He porosity. **c** Correlation between mass-based and susceptibility-based impregnation efficiency

(EMG807) or the oil-based ferrofluid (EMG 905). 20 out of 38 specimens show K_{min} axes of the AMFFS ellipsoid oriented parallel with K_{min} axes of the rock, independent of outcrop. Five specimens impregnated with water-based ferrofluid show an inverse fabric, which means that the K_{max} and K_{min} axes are exchanged compared to the unimpregnated specimens, and in six specimens (three water-based, three oil-based) K_{int} and K_{min} axes are exchanged (supplementary material 4). Inverse fabrics occur when magnetite particles are so small that superparamagnetic behaviour occurs. For magnetite, the single domain—superparamagnetic critical size limit occurs around 25–30 nm (Dunlop and Özdemir 1997).

Good or bad clustering of AMS and AMFFS fabrics is not related to mass or susceptibility impregnation efficiency nor to high or low permeability or porosity of the specimens (Table 3).

The strongest scattering between AMS and AMFFS was observed in specimens from the Lower Buntsandstein, which are characterized by high porosities, high permeabilities, the highest amount of quartz as detrital grains and the lowest

magnetic susceptibility. A larger scattering is also observed in specimens of hand sample R4, R5 and R7 from the Lower Rotliegend. All these specimens are also characterized by high porosities comparable to specimens from the Lower Buntsandstein (Fig. 2).

Discussion

Ferrofluid porosity compared to He porosity and impregnation efficiency

Since in the 1990s magnetic pore fabrics have been proposed as fast and efficient method to predict permeability anisotropy and flow directions in rocks (Pfleiderer and Halls 1990, 1994), its application was rare due to the large data variability, which made the interpretation often difficult and not clear. In the last couple of years, this method gained new attention (e.g., Robion et al. 2014; Parés et al. 2016) and modeling and theoretical studies were performed by Biedermann (2019), Biedermann et al. (2021), Pugnetti et al.

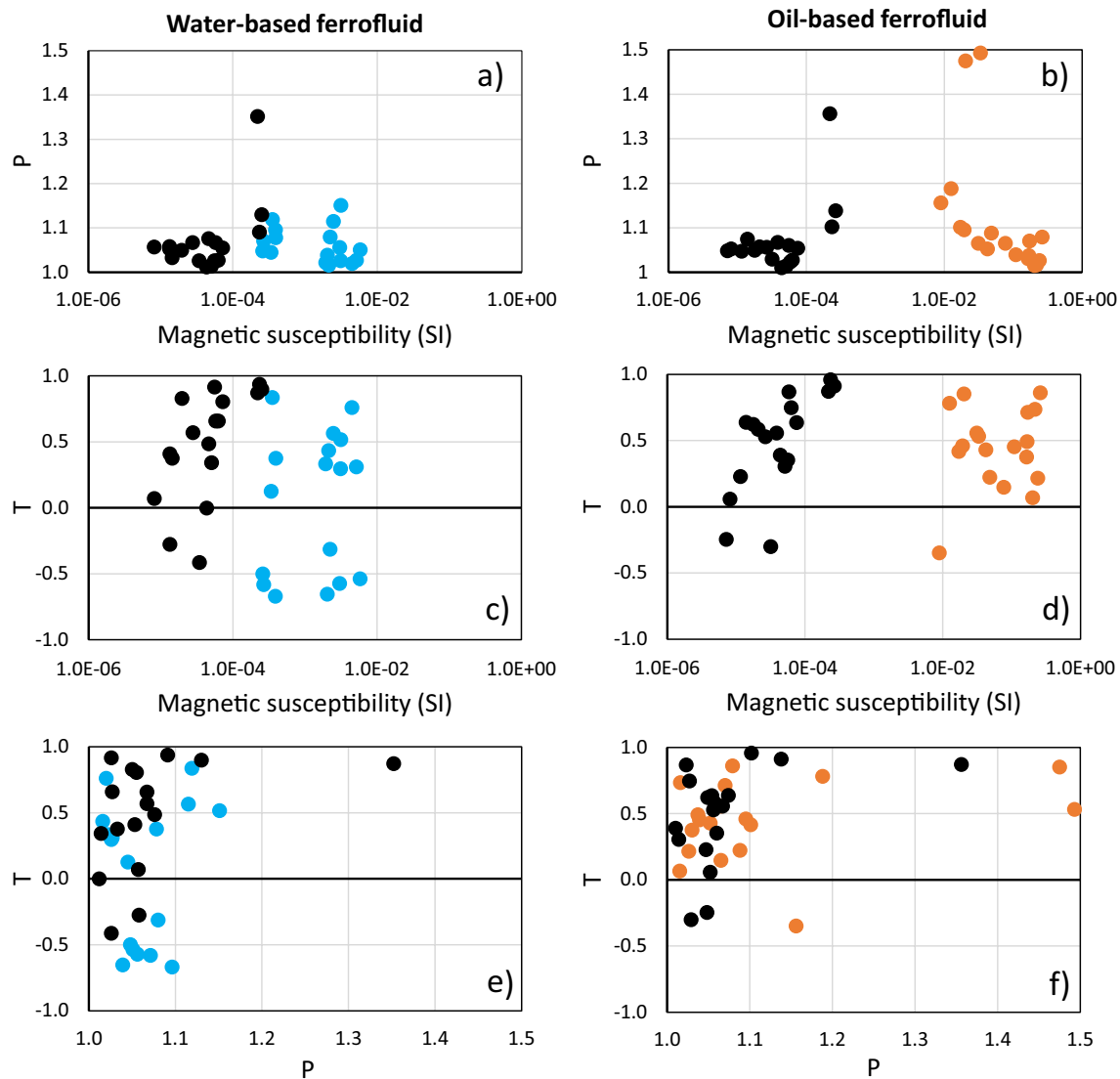


Fig. 7 AMS shape parameter versus magnetic susceptibility for unimpregnated sandstones (black) and water-based ferrofluid impregnation (blue) on left side, and for unimpregnated sandstones (black) and oil-

based ferrofluid impregnation (orange) on right side. **a, b:** Degree of anisotropy (P) versus magnetic susceptibility. **C, d:** Shape factor (T) versus magnetic susceptibility. **(e) and (f)** T versus P

(2022), and Biedermann and Parés (2022) with the aim to better understand the parameters that control magnetic pore fabrics.

Helium porosity data from this study agrees with those reported by Busch et al. (2022b) for the Lower Buntsandstein, Kleiner (2003) for the Upper Buntsandstein, and Aretz (2016) and Altenbockum et al. (2018) for the Rotliegend sandstones. According to Levorsen (1967) only samples with porosity > 15% and permeability > 10 mD indicate good to very good storage capacity properties. Our study has shown that He porosity for all specimens is always higher or equal to ferrofluid porosity (Fig. 4). The mean deviation between He porosity and ferrofluid porosity is 6.6% for oil-based, and is slightly lower with 3.0% for water-based ferrofluid

impregnation, although mass impregnation and susceptibility impregnation efficiency is similar for oil and water-based ferrofluid (Fig. 6). This means that on average ca. 5% of the pores were not reached by the ferrofluid due to pore or pore throat sizes below 10 nm, which is the approximate size of the magnetite particles in the ferrofluid, or due to incomplete impregnation of the pore network due to other reasons like bad interconnectivity. However, the relatively good correlation between He and ferrofluid porosity indicates an interconnected porosity in all investigated specimens independent of low or high porosity and permeability, which is a prerequisite to determine pore fabric geometries. Mercury porosimetry has shown that the pores can be classified as sub-capillary micropores as all diameters are below

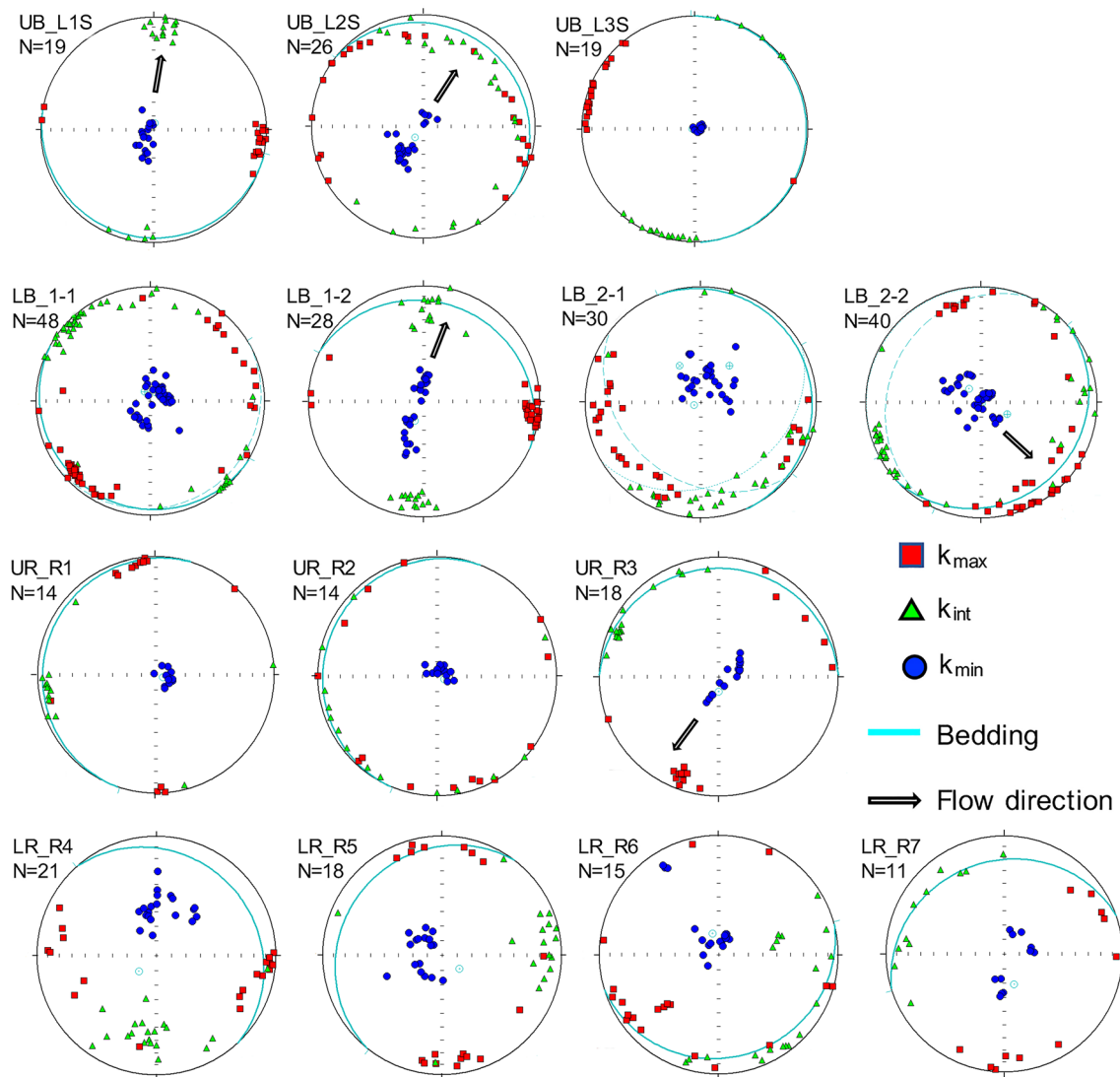


Fig. 8 AMS fabrics in stereographic projection with Kmin (blue), Kint (green) and Kmax (red) axes of unimpregnated sandstone specimens from the Lower Rotliegend (LR), Upper Rotliegend (UR), Lower

Buntsandstein (LB) and Upper Buntsandstein (UB). Bedding is shown as blue circle and arrows indicate flow directions, deduced from sedimentary observations and AMS axes orientation

0.4 mm, which is confirmed by 2D sediment petrographic studies (Fig. 2), and therefore interconnectivity of pores should be good.

A first indication of a good impregnation efficiency of the absorbed ferrofluid is the good correlation between He and ferrofluid porosity (Fig. 5b) (Louis et al. 2003). This good correlation is also confirmed by the positive correlation between mass of the ferrofluid and magnetic susceptibility (Fig. 5a) suggesting a rather successful impregnation process. One specimen impregnated with water-based ferrofluid has been cut vertically into half for a thin section preparation, and this specimen has not shown visible differences in the ferrofluid distribution, confirming that the pore space was sufficiently filled by the ferrofluid. Significantly higher magnetic susceptibility of oil-based compared to

water-based ferrofluid of one magnitude has been observed as the oil-based EMG905 ferrofluid has a susceptibility of $97.12 \times 10^{-6} \text{ m}^3/\text{kg}$ (dilution 1:30) and the water-based EMG807 ferrofluid of $6.63 \times 10^{-6} \text{ m}^3/\text{kg}$ (dilution 1:10). This is surprising as the stronger diluted ferrofluid shows the higher magnetic susceptibility. A recent study by Biedermann et al. (2021) has shown that the effective susceptibility of different ferrofluids depends on the measurement frequency, however, FerroTec does not provide the measurement frequency. Therefore, magnetic susceptibility of ferrofluid used for magnetic pore fabric studies should be always measured under the same conditions as the AMFFS measurements as suggested by Biedermann et al. (2021).

An important quality factor for the interpretation of magnetic pore fabrics is the impregnation efficiency, which is the

Table 5 Mean magnetic susceptibility and magnetic directional data from specimen used for water-based ferrofluid (EMG807) impregnation

Specimen	Kmean	P	T	Kmax_Dec	Kmax_Inc	Kint_Dec	Kint_Inc	Kmin_Dec	Kmin_Inc
UB_L1-12-1S	3,43E-05	1,025	-0,410	101,6	6,3	10,8	7,1	232,6	80,5
UB_L1-12-1S	3,54E-04	1,107	0,836	267,6	5,8	176,8	7,6	34,7	80,4
UB_L2-3-2S	5,81E-05	1,063	0,657	33,6	19,9	130	17,1	257,6	63,3
UB_L2-3-2S	3,40E-04	1,045	0,126	81,7	19,8	349,6	5,6	244,6	69,4
UB_L3-1-2S	7,24E-05	1,049	0,805	283	4,5	192,9	1,4	85,7	85,3
UBL3-1-2S	2,59E-04	1,046	-0,500	165,2	3,3	257,5	34,4	70,4	55,4
LB_1-1-1-2	1,34E-05	1,052	0,409	276,8	23,9	14,4	16,5	135,7	60,3
LB_1-1-1-2	2,10E-03	1,035	0,924	205	27,9	105,1	18	346,4	55,9
LB_1-1-3-2	1,96E-05	1,045	0,831	67,8	13,2	336,2	6,7	220	75,1
LB_1-1-3-2	3,89E-04	1,089	-0,669	83,6	79,1	321,3	5,9	230,4	9,2
LB_1-2-12-3	1,34E-05	1,057	-0,279	99	5,3	7,9	11,6	213,4	77,2
LB_1-2-12-3	2,68E-04	1,067	-0,582	197,3	71,8	324,8	11,3	57,7	14,1
LB_1-2-3-2	8,16E-06	1,057	0,067	46,7	1,8	139,1	53,8	315,4	36,1
LB_1-2-3-2	4,21E-03	1,032	0,887	151,9	21,4	38,5	45,4	259	36,8
LB_2-1-27-1	1,57E-05	1,050	0,529	230,4	17,1	130,2	29,9	346,1	54,6
LB_2-1-27-1	2,96E-04	1,059	-0,086	313,8	65	209	6,8	116	23,9
LB_2-1-9-1	1,45E-05	1,032	0,380	123,5	12,6	215,8	10	343,1	73,9
LB_2-1-9-1	4,87E-03	1,039	0,338	54,8	14,2	146	4,6	253,5	75
LB_2-2-18-1	2,79E-05	1,063	0,567	334,7	16,2	242,9	6	133,1	72,7
LB_2-2-18-1	3,93E-04	1,076	0,376	332,5	18,5	107,6	64,8	236,8	16,6
LB_2-2-6-1	4,64E-05	1,073	0,485	142,7	1,2	232,7	0,5	344,8	88,7
LB_2-2-6-1	2,00E-03	1,037	0,227	153,5	1	63,4	4,2	257,3	85,7
LB_2-3-4	2,17E-05	1,079	-0,013	271	21	180	1	87	69
LB_2-3-4	5,59E-03	1,012	0,573	191,4	42,8	73,3	27	322,2	35,2
UR_R1-1-1	2,53E-04	1,114	0,898	179	2	63	10	79	79
UR_R1-1-1	2,23E-03	1,079	-0,314	332	1	63	8	232	82
UR_R2-2-2S	2,34E-04	1,080	0,939	151	1	241	6	49	84
UR_R2-2-2S	2,04E-03	1,036	-0,654	324	4	234	2	114	85
UR_R3-7-1P	2,21E-04	1,309	0,872	199	10	291	12	65	75
UR_R3-7-1P	5,82E-03	1,049	-0,537	178	10	275	35	75	53
LR_R4-3-1S	4,33E-05	1,012	-0,010	93	9	188	27	346	62
LR_R4-3-1S	3,02E-03	1,053	-0,573	299	3	34	53	207	37
LR_R5-8-1P	5,08E-05	1,013	0,343	191	12	96	25	304	63
LR_R5-8-1P	3,13E-03	1,144	0,516	302	26	109	63	209	5
LR_R6-3-2S	5,57E-05	1,023	0,910	226	11	135	5	21	78
LR_R6-3-2S	2,48E-03	1,109	0,564	114	21	209	14	330	65
LR_R7-6-1P	6,28E-05	1,025	0,658	179	15	273	12	39	71
LR_R7-6-1P	3,11E-03	1,026	0,297	332	7	235	43	69	46

Kmean given in SI. *White* unimpregnated specimen. *grey* ferrofluid-impregnated specimen

Table 6 Mean magnetic susceptibility and magnetic directional data from specimen used for oil-based ferrofluid (EMG905) impregnation

Specimen	Kmean	P	T	Kmax_Dec	Kmax_Inc	Kint_Dec	Kint_Inc	Kmin_Dec	Kmin_Inc
UB_L1-1-1S	3,19E-05	1,029	-0,299	213	11	304	2	41	78
UB_L1-1-1S	1,25E-02	1,170	0,782	105	10	12	13	230	73
UB_L2-6-4S	5,59E-05	1,058	0,352	304,8	1	35,2	20,3	212,2	69,6
UB_L2-6-4S	1,72E-02	1,098	0,417	341,5	0,9	246,5	79,9	71,7	10,1
UB_L3-2-2S	7,52E-05	1,051	0,638	278,8	5,8	188,6	2,6	74,4	83,7
UB_L3-2-2S	3,33E-02	1,467	0,532	2,4	9,9	94,1	9,7	227,9	76,1
LB_1-1-4-1	1,15E-05	1,046	0,231	81,8	7,9	349,5	16,4	196,7	71,7
LB_1-1-4-1	1,09E-01	1,038	0,453	186,7	29,6	288,9	20,5	48,3	52,8
LB_1-1-8-1	2,09E-05	1,054	0,583	92,6	13,7	0,8	7,4	243,3	74,4
LB_1-1-8-1	3,19E-02	1,064	0,700	179,3	22,2	85,2	10,1	332,3	65,4
LB_1-2-2-2	8,12E-06	1,053	0,055	26,1	9,3	135	63,2	291,7	24,9
LB_1-2-2-2	1,65E-01	1,029	0,376	22,9	46,7	140,5	23,6	247,5	33,8
LB_1-2-8-1	8,07E-06	1,035	0,157	204	18,1	84,5	56,5	303,6	27,2
LB_1-2-8-1	4,27E-02	1,050	0,520	301,8	70,5	161,9	15,2	68,6	12
LB_2-1-12-1	1,78E-05	1,046	0,622	88,2	8,5	179,6	9,5	317,2	77,2
LB_2-1-12-1	4,90E-02	1,093	0,267	212,6	8,2	303,3	4,4	61,1	80,7
LB_2-1-18-1	2,66E-05	1,054	0,530	264,7	14	172,1	10,2	47,1	72,5
LB_2-1-18-1	2,18E-01	1,015	0,735	268,9	19,1	163,2	38,1	19,7	45,7
LB_2-2-2-1	3,85E-05	1,064	0,559	151,8	3,3	241,9	1,4	354,2	86,4
LB_2-2-2-1	1,97E-02	1,093	0,460	115,4	13,8	206,3	3,8	311,3	75,7
LB_2-2-27-2	1,40E-05	1,069	0,635	176,7	6,7	85,3	11,7	296,1	76,5
LB_2-2-27-2	2,02E-01	1,015	0,067	331,1	11	239,4	8,5	112,6	76
LB_2-3-3	1,88E-05	1,060	0,198	258	35	159	13	52	53
LB_2-3-3	4,81E-02	1,045	-0,128	259	16	165	14	34	68
UR_R1-3-2	2,67E-04	1,121	0,911	349,3	6,7	258,4	8,1	118,2	79,4
UR_R1-3-2	2,03E-02	1,417	0,852	5,5	5,3	274,6	10,4	122,2	78,3
UR_R2-10-3P	2,35E-04	1,089	0,958	249	5	159	10	5	79
UR_R2-10-3P	8,91E-03	1,153	-0,349	200,2	7,1	309,3	69,2	107,7	19,4
UR_R3-7-2P	2,19E-04	1,312	0,871	203	9	295	11	75	75
UR_R3-7-2P	2,62E-01	1,070	0,861	280,7	16	11,1	1,4	106	73,9
LR_R4-7-2P	4,37E-05	1,010	0,389	251	36	152	12	46	52
LR_R4-7-2P	2,40E-01	1,026	0,216	307,6	33	39,1	2,3	132,6	56,9
LR_R5-8-2P	5,11E-05	1,013	0,305	183	11	92	10	320	76
LR_R5-8-2P	7,70E-02	1,065	0,147	208,9	20,3	311,9	31,1	91,2	51,5
LR_R6-7-1P	5,83E-05	1,020	0,867	182	6	91	7	314	81
LR_R6-7-1P	1,68E-01	1,036	0,492	65,6	5,8	160,6	40,5	328,9	48,9
LR_R7-6-2P	6,28E-05	1,025	0,747	129	12	222	11	353	73
LR_R7-6-2P	1,72E-01	1,064	0,713	222,2	16,4	319	21,9	98,4	62,1

Kmean given in SI. *White* unimpregnated specimen, *grey* ferrofluid-impregnated specimen

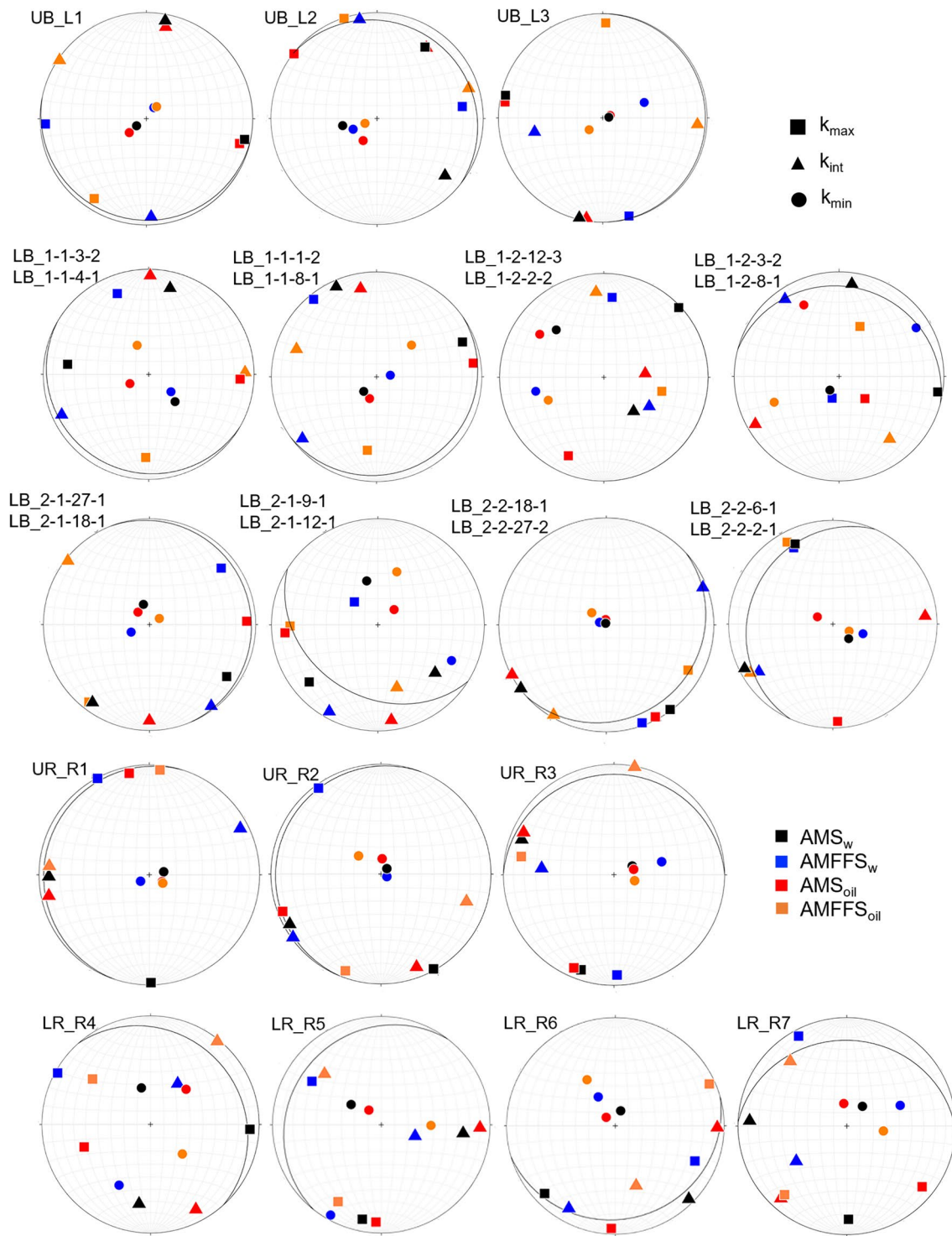


Fig. 9 Unimpregnated (AMS) and impregnated (AMFFS) sandstone specimens with bedding shown as great circle in stereographic projection. Each sphere shows magnetic fabrics of two specimens before

(AMS_w and AMS_{oil}) and after impregnation with water- ($AMFFS_w$) and oil-based ($AMFFS_{oil}$) ferrofluid. K_{min} (circle), K_{int} (triangle) and K_{max} (square)

measure for the percentage of pore space that is filled with ferrofluid (Biedermann et al. 2021; Pugnetti et al. 2022). If the ferrofluid fills the pore space as a homogeneous fluid

with constant density and susceptibility, the mass and susceptibility impregnation efficiency determined for the same specimen are expected to be the same (Pugnetti et al. 2022).

However, in accordance with other studies on porous sedimentary rocks (e.g., Robion et al. 2014; Parés et al. 2016; Pugnetti et al. 2022), we observed a significantly larger I.E.mass than I.E.susc (Fig. 6). Mass- and susceptibility-based estimates of impregnation efficiency deviate because mass changes are mostly controlled by the carrier liquid of the ferrofluid while the susceptibility increase is related to the magnetite nanoparticles themselves (Pugnetti et al. 2022). Therefore the I.E.susc seems to be best suited for the description of how many magnetite nanoparticles enter the pores. Especially the water-based ferrofluid impregnated specimens with prolate shapes and inverse fabrics show a low I.E.susc. The strong difference in susceptibility impregnation efficiency between water-based ferrofluid and oil-based ferrofluid (Fig. 6) with significantly higher values in the latter, clearly confirms earlier interpretations, according which oil-based ferrofluid is more suitable to impregnate rocks due to their better impregnation properties (e.g., Robion et al. 2014). However, the strong variation of I.E.susc compared to I.E.mass may suggest a significant heterogeneity of the magnetite nanoparticles in the pores. Furthermore, we have observed a less good concordance between He porosity and oil-impregnated ferrofluid porosity indicating some not yet solved problems during the impregnation process. Magnetic pore fabrics are interpreted to reflect a shape distribution that is related to a homogeneous dispersion of the magnetite nanoparticles carried by the non-magnetic carrier fluid in the pores. Biedermann et al. (2021) reported for synthetic samples with well-defined pore geometries several artefacts that may disturb a homogeneous distribution such as fluid films sticking to the surface of the specimens, gravity causing a deposition of magnetite nanoparticles at the bottom of each pore, particle clustering at magnetite (or other magnetic) grain surfaces in the rock, different wettability effects of minerals in the rock, and filtering effects due to narrow pore throats. These authors postulated that in addition to shape anisotropy the magnetic pore fabrics are characterized by a distribution anisotropy, which complicates their interpretation.

3D pore space from magnetic pore fabrics

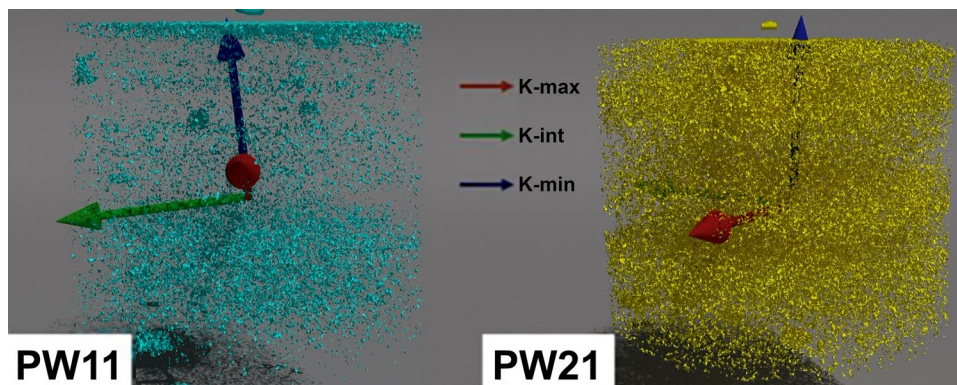
Primary sandstone fabrics are mainly controlled by the size, shape and mass of the detrital grains and the velocity of the medium in which they were transported (e.g., Talling and Hrouda 1993). The magnetic fabric of sandstones essentially reflects the preferred grain orientation of phyllosilicate minerals (mica grains, the phyllosilicate-rich rock fragments, laminated detrital matrix, and shale rock fragments). Another contribution to the magnetic fabric may result from the thin pigmented hematite coating around the quartz grains, although it is expected to be very small.

If we know the original orientation of the sample from the outcrop we are able to compare the magnetic pore fabric orientation to paleocurrent directions and sedimentary architecture (Pfleiderer and Halls 1990). Parés et al. (2016) investigated Triassic silty sandstones from the Iberian Range in Spain and found a very good correlation between AMS and AMFFS fabrics indicating that the pores have a preferred orientation parallel to bedding. These authors suggested that microporosity is controlled by the clay mineral fabric as the magnetic pore fabric mimics the rock fabric. They interpreted the preferred WNW-ESE orientation of Kmax axes as preferential fluid flow direction through these rocks.

In our study on Permo-Triassic sandstones from different Rotliegend and Buntsandstein facies from SW-Germany about 50% (20 out of 38) of the specimens show a good correlation between AMS and AMFFS fabrics. This is especially true for the litharenites from the Upper Rotliegend facies, which are characterized by a high amount of phyllosilicate-rich metamorphic rock fragments, strongly oblate magnetic fabrics and mostly low He porosity and permeability (specimens UR_R1-_R2, exception is UR_R3 with high He porosity and permeability). In analogy to the study of Parés et al. (2016), N-S oriented Kmax axes may be interpreted as the preferred fluid flow direction in the northern part of the Saar-Nahe Basin.

In all other samples, detrital quartz, feldspar, and rock fragments coated by hematite and goethite and little clay

Fig. 10 Reconstruction of the distribution of void space using X-ray computed μ -tomography for specimen LB_1-1-8-1 (left) and LB_2-1-12-1 (right) from the Lower Buntsandstein with colored arrows indicating the principal AMFFS axes



and carbonate cements dominate. Therefore, the pore space is likely not significantly dominated by the microporosity of the clay minerals but by the intergranular porosity between the detrital grains.

Interestingly, the lithic arkoses and feldspathic litharenites from the Upper Buntsandstein also show a very good correlation between AMS and AMFFS fabrics (see UB specimens in Fig. 9, Tables 5, 6). Again, these samples show low He porosity and permeability, the highest amount of cementation and initially low to intermediate magnetic susceptibility. The AMS fabric is likely related to detrital mica flakes, which are oriented parallel to bedding, siderite cements formed in the intergranular pores and hematite and goethite coatings around detrital quartz and feldspar grains. Therefore, the magnetic pore fabrics mimic the primary sedimentary fabrics with flow directions mostly NNE-oriented, or diagenetic fabrics of the sandstones. Bourquin et al. (2009) also reported paleocurrent directions generally oriented towards NNE for the Triassic sediments of the south-western part of the Germanic Basin.

Lower Buntsandstein subarkoses show magnetic rock fabrics, that seems to be related to imbrication of detrital grains and cross bedding, typical for braided river formations in the Buntsandstein deposits (Bourquin et al. 2009). These rocks show the lowest magnetic susceptibilities indicating the lowest amount of Fe-bearing minerals (mainly clay minerals and hematite and goethite dust rims) in agreement with sediment petrographic observations, and display high porosities and permeabilities. In these specimens, the largest differences between AMS and AMFFS were observed. This behavior is understandable in view of the high intergranular porosities, which are probably not homogeneously filled by the ferrofluid. Figure 10 shows X-ray computed μ -cT images for the specimen LB_1-1-8-1 (which also shows a deviation between AMS and AMFFS, red and orange square in Fig. 9), and LB_2-1-12-1 (which showed a good correlation between AMS and AMFFS; red and orange squares in Fig. 9). Both specimens were impregnated with oil-based ferrofluid. The images in Fig. 10 clearly show a layer-by-layer distribution of the pore-network parallel to the bedding (specimen was drilled perpendicular to bedding). The AMFFS-axes in specimen LB_1-1-8-1 show a rotation of the magnetic foliation by around 10° from the bedding-parallel 3D porosity network. The reason could be the very low mass impregnation efficiency of 17.4% (Table 3), indicating that this specimen might not have been properly impregnated by the ferrofluid. Therefore, mass impregnation efficiency seems to be indeed a good indicator for the ferrofluid impregnation quality as suggested by Pugnetti et al. (2022). Furthermore, sample 1-1-8-1 shows larger pores in the top half of the sample (Fig. 10), indicative of dissolved carbonate cement nodules (Busch et al. 2022b), which, when filled with ferrofluid, can distort the principal axes of the AMS ellipsoid.

A stronger difference between AMS and AMFFS fabric also occurs in subarkoses and sublitharenites from the Lower Rotliegend. These sandstones are characterized by mostly intermediate porosities and permeabilities and intermediate magnetic susceptibilities comparable to those from the Upper Buntsandstein. Here, magnetic rock fabric deviates in some samples from the bedding, suggesting a stronger diagenetic or even some tectonic overprint, which causes magnetic subfabrics. Most of the ferrofluid-impregnated specimens show magnetic foliation parallel to the rock magnetic fabric / bedding, but there is mostly no clear preferred orientation of K_{max} in the magnetic foliation plane. In most investigated thin sections, there is also no well preferred orientation of pore long axes in the bedding plane (Fig. 2), which implies a random movement of fluids within these planes. This agrees with a round shape of the detrital quartz grains and a missing preferred orientation of minerals in the bedding plane in most of the investigated sandstones.

The exchange of principal magnetic susceptibility axes before and after ferrofluid impregnation can thus be caused either by the very low anisotropy of the pore space or the behaviour of the magnetic ferrofluid in the pores. Modelling of Biedermann (2019) has shown that both, shape and distribution anisotropy, are needed to explain the magnetic pore fabrics of pore assemblies like those observed in sandstones. This author argues that effects of different types of anisotropy are complex and depend on factors like the shape of individual pores, the arrangement of pores and the spacing between them. It needs to be known if the ferrofluid acts as a homogeneous fluid throughout the pore space of a rock, or if the particles are concentrated at grain-pore interfaces, or cluster around certain minerals, e.g., those minerals with specific wettability or magnetic properties. The wettability of a mineral depends on its surface charge and can be measured by the contact angle on the mineral-fluid interface. E.g. for quartz the contact angle is higher for water-based ferrofluid (41°) than for kerosene-based fluid (30°) (Jakabsky et al. 2000).

The exchange of K_{min} with K_{max} axes (inverse fabrics) or the K_{int} axes (in oblate specimens) in the AMFFS fabrics may indicate a non-homogeneous distribution of the nm-sized magnetite particles in the pores with no substantial magnetic interaction. This would be an indication for a distribution anisotropy as postulated by Biedermann (2019).

Although there are still obstacles in the interpretation of magnetic pore fabrics, our study clearly shows that this method is very helpful for the directional characterization of 3D-pore networks as the weak 3D rock fabric (the grain's preferred orientation) of e.g., sandstones is enhanced by the ferrofluid, as the orientation of grains defines the available intergranular pore spaces. In sandstone reservoirs two types of fluid pathways can be distinguished. These are either

structurally controlled major fault zones and their associated fracture corridors as e.g., described by Reinhold et al. (2016) for Upper Buntsandstein sandstones in the Alsace, France, or those controlled by sedimentary or diagenetic processes. Haffen et al. (2013) suggested that playa-lake and fluvio-aeolian marginal desert facies (erg or sand sea) are better suited for fluid flow than braided river formations, even if they show high matrix permeability like those we have investigated from the Lower Buntsandstein. The reason is the drastic reduction of matrix connectivity due to oblique clayey layers. Therefore, magnetic pore fabric investigations always have to be backed up by other petrophysical investigations like porosity and permeability measurements, and sediment petrographic investigations, and have to be interpreted in a wider geological context.

Conclusions

In this study, we have applied the anisotropy of magnetic susceptibility using water- and oil-based ferrofluid impregnation for different Permo-Triassic sandstones of different Buntsandstein and Rotliegend facies, which represent Central Europe's highest geothermal water and hydrocarbon reservoir potential. We compared ferrofluid porosity with He porosity and permeability measured on the same specimen and correlated the magnetic pore fabric with rock fabric and sediment petrographic observations. We have measured a mean difference between He porosity and ferrofluid porosity of 3–6.5%, which we interpret as an indication of interconnected porosity and permeability, a prerequisite to determine pore fabric geometries. However, an important factor for the impregnation quality is the impregnation efficiency, a description of how many magnetite nanoparticles enter the pores (Biedermann et al. 2021; Pugnetti et al. 2022). We found that mass-based impregnation efficiency for water- (EMG807) and oil-based ferrofluid (EMG905) is mostly > 30%, but that susceptibility-based impregnation efficiency is much better for the oil-based than the water-based ferrofluid although the latter shows a higher difference between He and ferrofluid porosity. On the other side, specimens that were impregnated with water-based ferrofluid show deviating shapes of the AMFFS-ellipsoids as they tend to show more prolate shapes and inverse fabrics.

The AMS of the different unimpregnated sandstone types show oblate and triaxial shapes and reflect well defined primary sedimentary to diagenetic fabrics (Table 4). Grain imbrication and cross bedding along with more laminated sedimentary structures are common and are reflected in the distribution of the AMS axes. The magnetic pore fabrics mostly mimics this primary sedimentary fabric and deviation in axes orientation can be related either to the low anisotropy < 1.07 in sandstones from the Lower and Upper Buntsandstein, or a low impregnation efficiency. In agreement with sediment

petrographic investigations there is mostly no preferred orientation of the pore long axes within the bedding plane. This observation agrees with temperature gradient logs published by Haffen et al. (2013) for Buntsandstein sandstone formations drilled by the Soultz-sous-Forêts borehole EPS-1 in the western part of the Upper Rhine Graben, France, which imply a bedding-parallel fluid flow connected through westward-dipping damage zones of the Soultz fault that connect the sediments with deeper hot fluid sources. Further magnetic pore fabric investigations near fracture corridors may help to delineate such zones. Our results have potential implications for sandstones and other rocks naturally percolated by hydrothermal fluids (Sizaret et al. 2003; Ejembi et al. 2020), and may be of interest for the hydrocarbon and mining industry or ocean sciences.

Supplementary Information The online version contains supplementary material available at <https://doi.org/10.1007/s00531-023-02352-z>.

Acknowledgements Thanks to Hagen Steger, Institute of Applied Geosciences, KIT, Germany for cooperation with mercury infiltration porosimetry, and to the two reviewers Harald Böhnelt and Eric Ferré for their constructive comments.

Funding Open Access funding enabled and organized by Projekt DEAL. The authors declare that they disclose financial or non-financial interests that are directly related to the work submitted for publication.

Data availability All data are included in this manuscript and supplement.

Open Access This article is licensed under a Creative Commons Attribution 4.0 International License, which permits use, sharing, adaptation, distribution and reproduction in any medium or format, as long as you give appropriate credit to the original author(s) and the source, provide a link to the Creative Commons licence, and indicate if changes were made. The images or other third party material in this article are included in the article's Creative Commons licence, unless indicated otherwise in a credit line to the material. If material is not included in the article's Creative Commons licence and your intended use is not permitted by statutory regulation or exceeds the permitted use, you will need to obtain permission directly from the copyright holder. To view a copy of this licence, visit <http://creativecommons.org/licenses/by/4.0/>.

References

- Aigner T, Bachmann GH (1992) Sequence-stratigraphic framework of the German Triassic. *Sed Geol* 80:115–135
- Altenbockum M, Berens K, Enzmann F, Kersten M, Rüde TR, Wieber GHE (2018) Fallbeispiel Kluftgrundwasserleiter – Charakterisierung eines Grundwasserleiters im Rotliegendesandstein des Saar-Nahe-Beckens *Grundwasser-Zeitschrift der Fachsektion Hydrogeologie*. *Grundwasser* 23:177–187. <https://doi.org/10.1007/s00767-017-0380-1>
- Aretz A, (2016) Aufschlussanalogstudie zur geothermischen Reservoircharakterisierung des Permokarbons im nördlichen Oberrheingraben., TU Darmstadt
- Backhaus E (1974) Limnische und fluviatile Sedimentation im südwestdeutschen Buntsandstein. *Geol Rundsch* 63:925–942

- Biedermann AR (2019) Magnetic pore fabrics: the role of shape and distribution anisotropy in defining the magnetic anisotropy of ferrofluid-impregnated samples geochemistry. *Geophys, Geosyst* 20:5650–5666. <https://doi.org/10.1029/2019GC008563>
- Biedermann AR, Parés JM (2022) Magnetic properties of ferrofluid change over time: Implications for magnetic pore fabric studies. *J Geophys Res Solid Earth*. <https://doi.org/10.1029/2022JB024587>
- Biedermann AR, Pugnetti M, Zhou Y (2021) Explaining the large variability in empirical Relationships between magnetic pore fabrics and pore Space properties. *Geophys J Int* 227:496–517. <https://doi.org/10.1093/gji/ggab230>
- Blackbourn GA (2012) Cores and Core Logging for Geoscientists. Whittles Publishing, Dunbeath, Scotland
- Bohnsack D, Potten M, Freitag S, Einsiedl F, Zosseder K (2021) Stress sensitivity of porosity and permeability under varying hydrostatic stress conditions for different carbonate rock types of the geothermal Malm reservoir in Southern Germany. *Geotherm Energy*. <https://doi.org/10.1186/s40517-021-00197-w>
- Bourquin S et al (2011) The Permian-Triassic transition and the onset of Mesozoic sedimentation at the northwestern peri-Tethyan domain scale: palaeogeographic maps and geodynamic implications Palaeogeography. *Palaeoclimatology, Palaeoecology* 299:265–280. <https://doi.org/10.1016/j.palaeo.2010.11.007>
- Bourquin S, Guillocheau F, Péron S (2009) Braided rivers within an arid alluvial plain (example from the Lower Triassic, western German Basin): recognition criteria and expression of stratigraphic cycles. *Sedimentology* 56:2235–2264. <https://doi.org/10.1111/j.1365-3091.2009.01078.x>
- Bourquin S, Péron S, Durand M (2006) Lower Triassic sequence stratigraphy of the western part of the Germanic Basin (west of Black Forest): Fluvial system evolution through time and space. *Sed Geol* 186:187–211. <https://doi.org/10.1016/j.sedgeo.2005.11.018>
- Busch A et al (2017) Determining the porosity of mudrocks using methodological pluralism Geological Society. London, Special Publications 454:15–38. <https://doi.org/10.1144/sp454.1>
- Busch B, Adelmann D, Herrmann R, Hilgers C (2022a) Controls on compactional behavior and reservoir quality in a Triassic Buntsandstein reservoir, Upper Rhine Graben. *SW Germany Marine and Petroleum Geology* <https://doi.org/10.1016/j.marpetgeo.2021.105437>
- Busch B, Hilgers C, Adelmann D (2020) Reservoir quality controls on Rotliegend fluvio-aeolian wells in Germany and the Netherlands, Southern Permian Basin – Impact of grain coatings and cements. *Mar Pet Geol*. <https://doi.org/10.1016/j.marpetgeo.2019.104075>
- Busch B, Spitzner A-D, Adelmann D, Hilgers C (2022b) The significance of outcrop analog data for reservoir quality assessment: A comparative case study of Lower Triassic Buntsandstein sandstones in the Upper Rhine Graben. *Mar Pet Geol*. <https://doi.org/10.1016/j.marpetgeo.2022.105701>
- Dachroth W (1985) Fluvial sedimentary styles and associated depositional environments in the Buntsandstein west of river Rhine in Saar area and Pfalz (F.R. Germany) and Vosges (France). In: Mader D (ed) *Aspects of Fluvial Sedimentation in the Lower Triassic Buntsandstein of Europe*, vol 4. Lecture Notes in Earth Sciences. Springer-Verlag, Heidelberg, pp 197–248
- Deutsche Stratigraphische Kommission (2016) *Stratigraphische Tabelle von Deutschland 2016*.
- Dunlop DJ, Özdemir Ö (1997) *Rock magnetism - fundamentals and frontiers*. Cambridge studies in magnetism. Cambridge University Press.
- Ejemi JI, Ferré EC, Satolli S, Friedman SA (2020) Post-depositional fluid flow in Jurassic sandstones of the Uncompahgre uplift: insights from magnetic fabrics front. *Earth Sci* 8:601415. <https://doi.org/10.3389/feart.2020.601415>
- Feist-Burkhardt S et al. (2008) Triassic. In: McCann T (ed) *The Geology of Central Europe Volume 2: Mesozoic and Cenozoic*. Geological Society of London, pp 749–821. doi: <https://doi.org/10.1144/cev2p.1>
- Folk RL (1980) *Petrology of Sedimentary Rocks*. Hemphill Publishing Company, Austin, Texas, USA.
- Frey M, Bär K, Stober I, Reinecker J, Jvd V, Sass I (2022) Assessment of deep geothermal research and development in the Upper Rhine Graben. *Geothermal Energy* 10:18. <https://doi.org/10.1186/s40517-022-00226-2>
- Geluk M, McKie T, Killhams B (2018) *An introduction to the Triassic: current insights into the regional setting and energy resource potential of NW Europe* Geological Society. London, Special Publications 469:139–147. <https://doi.org/10.1144/SP469.1>
- Haffen S, Géraud Y, Diraison M, Dezayes C Fluid-flow zones in a geothermal sandstone reservoir: Localization from thermal conductivity and temperature logs, borehole EPS1 (Soultz-sous-Forêts, France) and 3D models. In: *Thirty-Eighth Workshop on Geothermal Reservoir Engineering*, Stanford University, Stanford, California, 2013.
- Henk A (1993) Late orogenic basin evolution in the Variscan inter-nides: the Saar-Nahe Basin, southwest Germany. *Tectonophysics* 223:273–290. [https://doi.org/10.1016/0040-1951\(93\)90141-6](https://doi.org/10.1016/0040-1951(93)90141-6)
- Hrouda F, Hanak J, Terzijski I (2000) The magnetic and pore fabrics of extruded and pressed ceramic models. *Geophys J Int* 142:941–947
- Jakabsky S, Lovas M, Mockovciakova A, Hredzak S (2000) Utilization of ferromagnetic fluids in mineral processing and water treatment. *J Radioanal Nucl Chem* 246:543–547
- Kleiner S, (2003) Untersuchungen zur Optimierung von Erdwärmesondenanlagen– petrophysikalische Messungen und numerische Simulationen. RWTH Aachen
- Knopp J, Steger H, Moormann C, Blum P (2022) Influence of weathering on pore size distribution of soft rocks. *Geotech Geol Eng* 40:5333–5346. <https://doi.org/10.1007/s10706-022-02217-3>
- Levorsen AI (1967) *Geology of Petroleum*. W.H. Freeman Company.
- Loucks RG, Reed RM, Ruppel SC, Hammes U (2012) Spectrum of pore types and networks in mudrocks and a descriptive classification for matrix-related mudrock pores. *AAPG Bull* 96:1071–1098. <https://doi.org/10.1306/08171111061>
- Louis L, David C, Robion P (2003) Comparison of the anisotropic behaviour of undeformed sandstones under dry and saturated conditions. *Tectonophysics* 370:193–212
- Nabawy BS, Rochette P, Géraud Y (2009) Petrophysical and magnetic pore network anisotropy of some cretaceous sandstone from Tushka Basin. *Egypt Geophys J Int* 177:43–61
- Parés JM, Miguens L, Saiz C (2016) Characterizing pore fabric in sandstones with magnetic anisotropy methods: Initial results. *J Petrol Sci Eng* 143:113–120. <https://doi.org/10.1016/j.petrol.2016.02.028>
- Pfleiderer S (1992) Magnetic pore fabric analysis.
- Pfleiderer S, Halls HC (1990) Magnetic susceptibility anisotropy of rocks saturated with ferrofluid: a new method to study pore fabric? *Phys Earth Planet Inter* 65:158–164
- Pfleiderer S, Halls HC (1994) Magnetic pore fabric analysis: a rapid method for estimating permeability anisotropy. *Geophys J Int* 116:39–45
- Pokorny JS, P.; Hrouda, F. (2004) Anisotropy of magnetic susceptibility of rocks measured in variable weak magnetic fields using the KLY-4S Kappabridge Geol Soc London (spec Publ):69–76
- Pugnetti M, Zhou Y, Biedermann AR (2022) Ferrofluid impregnation efficiency and its spatial variability in natural and synthetic porous media: implications for magnetic pore fabric studies. *Transp Porous Media* 144:367–400. <https://doi.org/10.1007/s11242-022-01809-0>
- Reinhold C, Schwarz M, Bruss D, Heesbeen B, Perner M, Suana M (2016) The northern upper Rhine graben : re-dawn of a mature petroleum province? *Swiss Bulletin Appl Geol*. <https://doi.org/10.5169/seals-658196>

- Rieckmann M, (1970) Untersuchung von Turbulenzerscheinungen beim Fließen von Gasen durch Speichergesteine unter Berücksichtigung der Gleitströmung *Erdoel-Erdgas-Zeitschrift* 86:36–51
- Robion P, David C, Dautriat J, Colombier J, Zinsmeister L, Collin P (2014) Pore fabric geometry inferred from magnetic and acoustic anisotropies in rocks with various mineralogy, permeability and porosity *Tectonophysics* 629:109–122
- Schneider CA, Rasband WS, Eliceiri KW (2012) NIH Image to ImageJ: 25 years of image analysis *Nature Methods* 9:671–675
- Schumacher ME (2002) Upper Rhine graben: role of preexisting structures during rift evolution. *Tectonics*. <https://doi.org/10.1029/2001tc900022>
- Sizaret S, Chen Y, Chauvet A, Marcoux E, Touray JC, (2003) Magnetic fabrics and fluid flow directions in hydrothermal systems. A case study in the Chaillac Ba^FFe deposits (France) *Earth and Planetary Science Letters* 206: 555–570 doi:0.1016/S0012-821X(02)01112-3
- Stollhofen H, (2007) Postvulkanische Rotliegend-Schwemmfächersysteme am Hunsrück-Südrand, Saar-Nahe-Becken, SW-Deutschland *Jahresberichte und Mitteilungen des Oberrheinischen Geologischen Vereins* 89: 285–306
- Tarling DH, Hrouda F (1993) *The magnetic anisotropy of rocks*. Chapman and Hall
- Taylor T, Lander RH, Bonnell LM, (2022) Sandstone Petrography, Petrology, and Modeling. In. *SEPM Concepts in Sedimentology and Paleontology*, 20. SEPM (Society for Sedimentary Geology). doi: <https://doi.org/10.2110/sepmcsp.13.06>
- Uyeda S, Fuller MD, Belshé JC, Girdler RW (1963) Anisotropy of magnetic susceptibility of rocks and minerals. *J Geophys Res* 69:279–291
- Ziegler PA (1992) European cenozoic rift system. *Tectonophysics* 208:91–111